

One-Dimensional Nanostructures for Neutron Detection

Mission Support

Dr. Yong Zhu

North Carolina State University

Suibel Schuppner, Federal POC

John Neal, Technical POC

DOE-NEUP Final Report for Award # 11-3225

“One-Dimensional Nanostructures for Neutron Detection”



By

PI: Yong Zhu

Co-PIs: Jacob Eapen and Ayman I. Hawari

Graduate Students: William Lowe, Guangming Cheng, Shanshan Yao

Postdoctoral Associates: Brahmananda Chakraborty

February 2015

This report consists of four parts in addition to a publication/presentation list. Part I is on electronic structure simulations on boron nitride (BN) and BC_xN nanotubes using density function theory (DFT), Part II is on fabrication and characterization of nanowire sensors, Part III is on irradiation response of BN nanotubes using molecular dynamics (MD) simulations, and Part IV is on the *in-situ* transmission electron microscopy (TEM) study of irradiation response of BN nanotubes.

Publications and Presentations

1. S. Yao and Y. Zhu, "Wearable multifunctional sensors using printed stretchable conductors made of silver nanowires", *Nanoscale* 6, 2345-2352 (2014).
2. J.D. Durham and Y. Zhu, "Fabrication of Functional Nanowire Devices on Unconventional Substrates using Strain-Release Assembly", *ACS Applied Materials & Interfaces* 5, 256-261 (2013).
3. G. Cheng, S. Yao, Y-K Yap and Y. Zhu, "Evolution of Irradiation-Induced Vacancy Defects in Boron Nitride Nanotubes", manuscript in preparation (2015).
4. B. Chakraborty and J. Eapen, "Effect of Li on the structure and band structure of boron-based nanotubes", manuscript in preparation (2014).
5. B. Chakraborty and J. Eapen, "Direct conversion neutron detection using functionalized boron nitride nanotubes", in Fall MRS Meeting, Boston, MA, Nov. 2011.
6. F. Xu, J. W. Durham and Y. Zhu, "Strain-Release Assembly of Nanowires on Stretchable Substrates", in ASME International Mechanical Engineering Congress and Exposition, Denver, CO, Nov. 2011.

Part I. Electronic Structure Simulations on BN and BC_xN Nanotubes using Density Functional Theory (DFT)

1. Introduction

We have investigated the structure and electronic properties of BN [1-4] and BC₄N [5] nanotubes using density functional theory (DFT) simulations. The interaction between boron and neutron produce Li which has the potential to destabilize the structure as well as adversely affect the electronic properties. We have observed that addition of Li reduces the band gap of BNNT and BC₄N nanotubes and makes them almost metallic. To prevent the reduction of band gap and to maintain structural integrity, we have proposed adding dopants in the nanotubes prior to irradiation with neutrons. We have successfully identified several dopants (F, O, Cl) which can retain the semiconducting and structural properties of BC₄N nanostructures.

In addition to BN NT, another promising nanostructure material for neutron detection is the BC₄N nanotube (BC₄N NT). BC₄N nanotube brushes have been synthesized by the high temperature reaction of amorphous carbon nanotube (a-CNT) brushes with a mixture of boric acid and urea [5]. The most stable structure is predicted to be the one where BN₃ and NB₃ units are connected by a B–N bond. The ground-state structures of BC₄N nanotubes having different chirality; configurations (6,0) and (8,0) zigzag nanotubes, and (6,6) armchair nanotube have been reported to be semi conducting with various energy gaps. The (6,6) armchair BC₄N nanotube shows the largest band gap (1.0 eV). The thermal stability of the BC₄N nanotube is very high (up to 900 K); the presence of B and N makes this system more stable compared to the well-known carbon nanotube.

Lithium produced due to interaction of boron and neutron modifies the structure and the electronic properties of the nanotube material. After losing its energy, Li can be absorbed in the vacant sites (e.g., N or B in BN NT or N, B or C in BC₄N NT, or absorbed as an adatom in various parts of the nanotube system. So the nanostructure material which is initially suitable for direct conversion neutron detection can deteriorate after the accumulation of lithium. Our strategy in this study is to tailor the initial configuration such that the accumulation of lithium does not alter the properties. In this annual report we present the structure and electronic properties of pure BN NT and BC₄N nanotubes, followed by an investigation on the effect of lithium (as adatoms and substitutional dopants in both BN NT and BC₄N NT). Finally we tune the properties of (BNNT + Li) and (BC₄N NT + Li) systems by adding appropriate dopants to negate the adverse effects of lithium.

2. Methodological Details

In this work, we have taken a (8, 0) zigzag BN NT nanotube having a length twice of its lattice constant and placed in a 20 Å × 20 Å × 8.6 Å tetragonal supercell. For the simulation of BC₄N nanotube, (6,6) chirality with 72 atoms was considered. All the calculations were carried out using density functional theory based plane wave pseudopotential methods as implemented in the VASP code [6-9]. The projector augmented wave (PAW) pseudopotentials were used with 400 eV cut-off for plane-wave basis expansion with generalized gradient approximations (PBE-GGA) of Perdew et al. [10] for the exchange-correlation term. Monkhorst-Pack special k point scheme was used with 11 k points along the tube axis for Brillouin-zone integration [11]. The atomic positions were relaxed using conjugate gradient methods until the force on each atom

becomes less than 1 meV/Å. Using relaxed structure of BN NT and BC₄N nanotubes we then carried out the total-energy calculations. Similar studies were done for BN NT and BC₄N NT with and without dopants.

3. Results and Discussion

3.1 Study on Pristine and Doped BN NT

First we report the structure and electronic properties of the perfect boron nitride nanotube [1] (BN NT) through first principles investigations and compare our results with the reference data for perfect BN NT. Initially, BN NT of chirality (8,0) was placed in the middle of the supercell and the system was allowed to relax. The relaxed structure is shown in the Fig. 1. The average B-N Bond length for the pristine BN NT is 1.457 Å which is in good agreement with earlier reported results [12]. The angle in the ring is 120.0° degree as expected. Figure 2 shows total Density of States (DOS) for perfect BN NT. From the Fig. 2 the band gap for the (8,0) BNNT is observed to 3.62 eV, which is in good agreement with the value 3.65 eV reported for the BN NT of same chirality [4]. J. Wu et al. [13] predicted various band gap for various chiralities. They reported 4.02, 3.64, 4.19 and 4.36 eV band gap for the BN NT with chiralities (10,0), (6,2), (4,2) and (5,5) respectively. So, we can see that as the diameter reduces (lower chirality) the band gap of BN NT reduces. X. Blase et al. [14] predicted that for diameters greater than 9.5 Å all BN NTs except the (*n*, 0) tubes with *n* less than 12 the band gap is stabilized around 4 eV. Experimentally measured band gap for bulk hexagonal boron nitride is 5.8 eV [15]. The symmetry between the spin up and spin down states in Fig. 2 indicates that the perfect BN NT is non-magnetic in nature as expected.

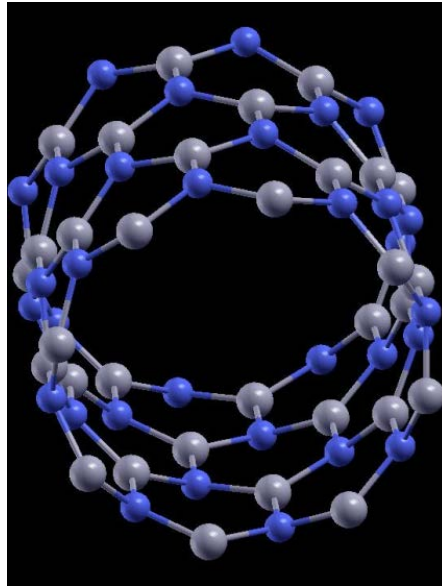


Figure 1. Relaxed structure of pristine (8,0) BNNT, average bond length= 1.457 Å, bond angle=120°, blue atoms are nitrogen.

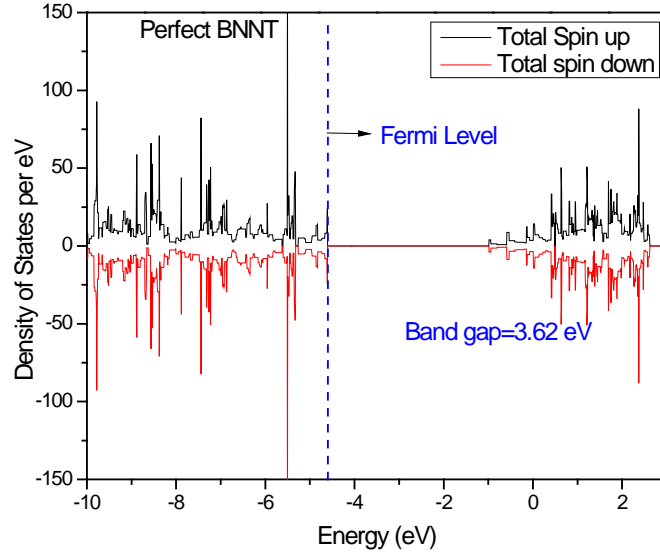


Figure 2. Total Density of States (DOS) for pristine (8,0) BN NT

Next we have considered substitution doping. The relaxed structure of pristine BN NT, carbon substituted BN NT in place of nitrogen and carbon substituted BN NT in place of boron are shown in the Fig. 3. Bond length is larger when C is doped in place of N compared to B replacement. Bond angle is less in case of N replacement compared to B replacement. As can be observed, the tube is deformed from the hexagonal structure. This deformation introduces magnetism in the C doped BN NT. Total density of states (DoS) for these three structures are plotted in Fig. 4. Band gap reduces with C doping. Reduction in Band gap is more when B is replaced by C. For boron replacement band gap reduces to 2.85 eV whereas for nitrogen substitution band gap comes out to be 3.33 eV. The desired band gap may be obtained by substituting more C atoms. Fig. 5 shows the relaxed structure of Ca doped BN NT. It can be seen that the Ca atom stays above the hexagonal plane. This results in the deformation of the hexagonal structure. Ca-B & Ca-N bond length is much higher than B_N (perfect), C_B(C doped) & C_N(C doped) length. Also Ca doping makes the system magnetic. For Ca doped (in place of N) magnetic moment is almost 1.0 Bohr magnetron (for the system considered). Fig. 6 shows density of states (DoS) for perfect (8,0) pristine BN NT, DoS for Ca doped BN NT in place of N and partial DoS of Ca atom in doped BN NT. The band gap is reduced from 3.62 eV to 0.62 eV, which may be desirable from a detector point of view. We can see from the graph (bottom) the prominent 3d states for Ca are near the Fermi level. Also spin up & spin down 3d states are around 1 eV below the Fermi level and around 1 eV above the Fermi level. We can also see prominent s state near Fermi level and the states above the Fermi level is populated by Ca d states. We can see similar DoS for BN NT+Ca (in place of N) and Ca (in BN NT) d states above the Fermi level. Appearance of those population in Ca doped BN NT reduces the band gap of perfect BN NT. We can also see p up and down states for Ca atom (in BN NT) around 1.5 to 4.5 eV.

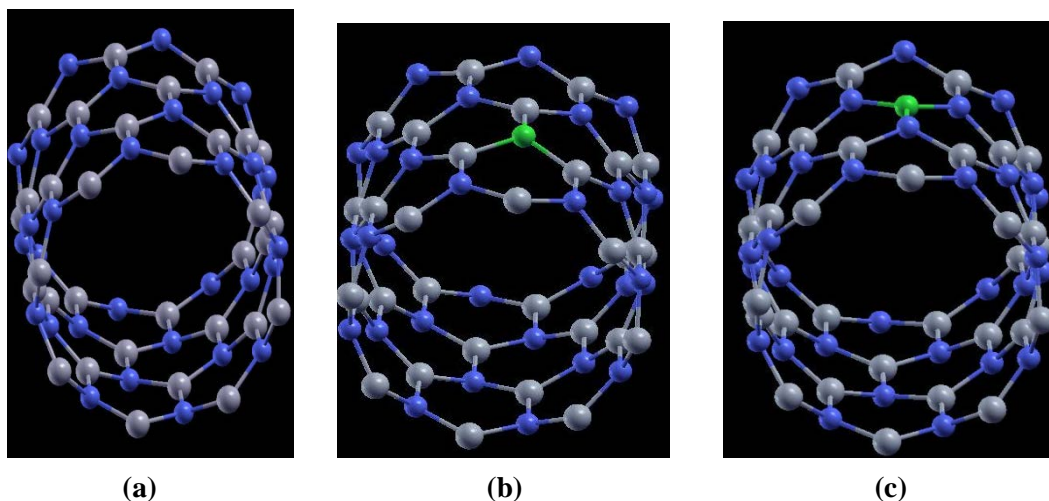


Figure 3. Relaxed structure of (a) pristine (8,0) BN NT, average bond length= 1.457 Å, bond Angle=120° (b) C substituted (N) BN NT; green atom is C; C-B bond length 1.52 Å, 1.52 Å and 1.50 Å; bond Angle (for C) 117.0°, 117.0° and 114.0 degree (c) C substituted(B) BN NT C-N; bond length 1.40 Å, 1.40 Å and 1.37 Å; bond angle (for C) 120.4°, 120.4° and 116.8°.

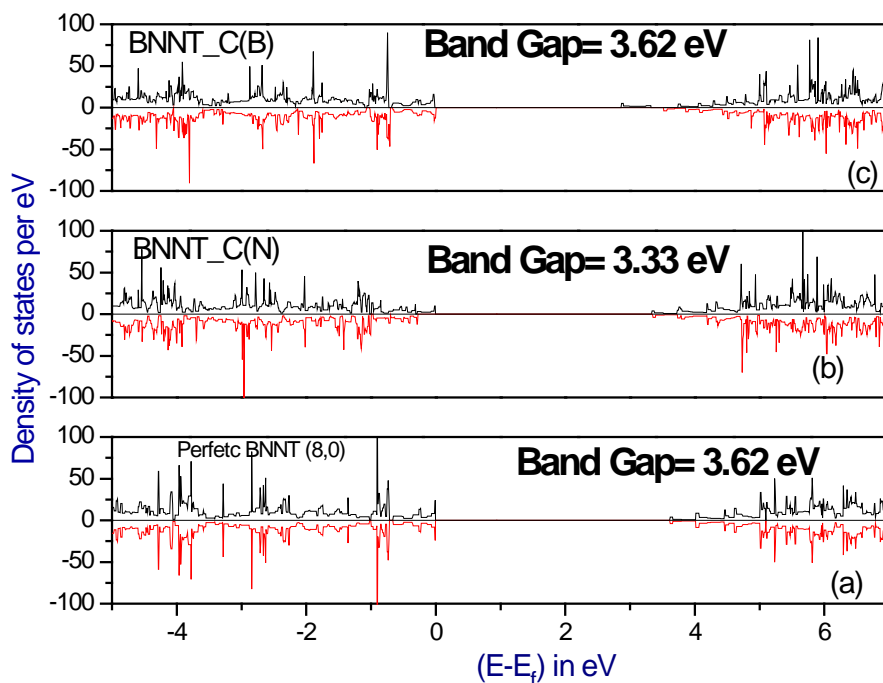


Figure 4. Total Density of States (DoS) for perfect (a) (8,0) pristine BN NT (b) C doped in place of N (c) C doped in place of B, The Fermi level is at zero.

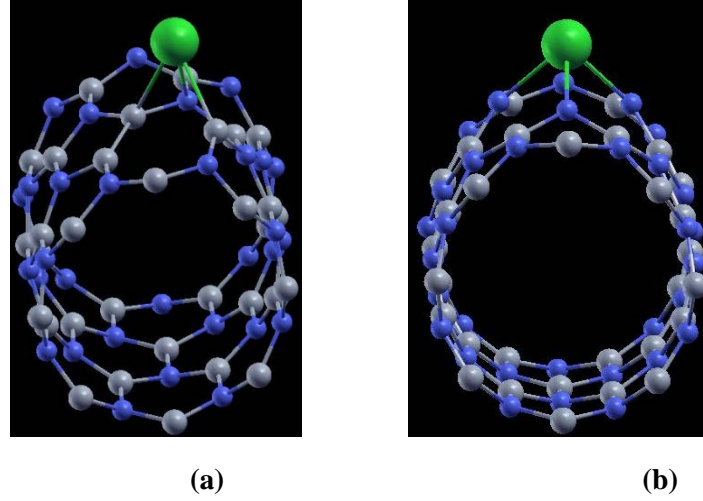


Figure 5. Relaxed structure of (a) Ca substituted (in place of nitrogen) BN NT; green atom is Ca; Ca-B bond length 2.56 Å, 2.53 Å & 2.58 Å; bond Angle (for Ca) 69.79°, 69.79° & 35.55° (b) Ca substituted (in place of boron) BN NT; Ca-N bond length 2.21 Å, 2.21 Å & 2.24 Å; bond angle (for Ca) 78.35°, 78.35° & 91.80°.

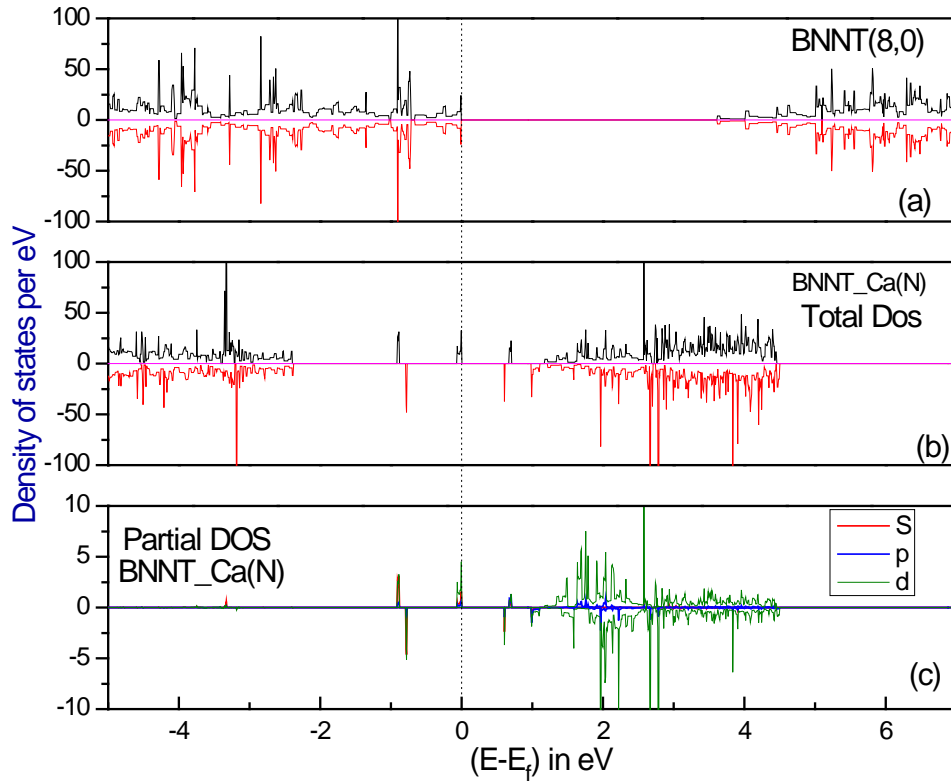


Figure 6. Density of States (DoS) for perfect (a) (8,0) pristine BNNT (b) Ca doped BNNT in place of N (c) Partial Dos of Ca atom in doped BNNT, Fermi level is at zero.

3.2 Study on perfect BC_4N nanotube

The various structure of BC_4N nanotubes are presented in Fig. 7. The most ordered structure is shown in Fig. 7(d) in which BN_3 and NB_3 units are linked with one B–N bond. For the present simulations we have considered (6,6) chirality tube for which band gap is around 1 eV. The relaxed structure of BC_4N nanotube is shown in Fig. 8. Fig. 9. Shows the total density of states (DoS) for perfect BC_4N nanotube. From Fig. 9 the band gap for the (8,6) BC_4N nanotube is observed to be around 1.0 eV.

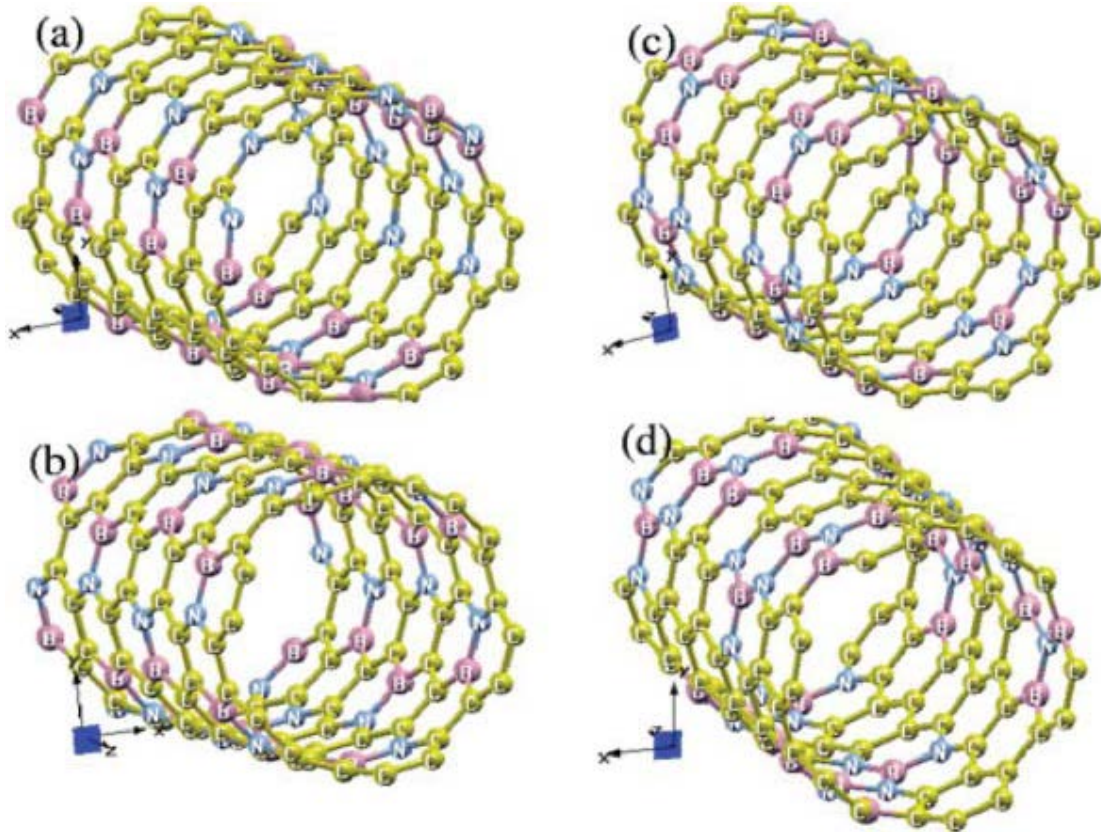


Figure 7. (6,6) BC_4N nanotubes: (a) a disordered structure D, in which carbon atoms occupy B and N sites in a BN NT randomly with a probability of 0, (b) an ordered structure S1, with one B–N bond present in each carbon ring, (c) an ordered structure S2, where BN_3 and NB_3 units are distributed on alternate C_6 rings, and (d) an ordered structure S3, in which BN_3 and NB_3 units are linked with one B–N bond [5].

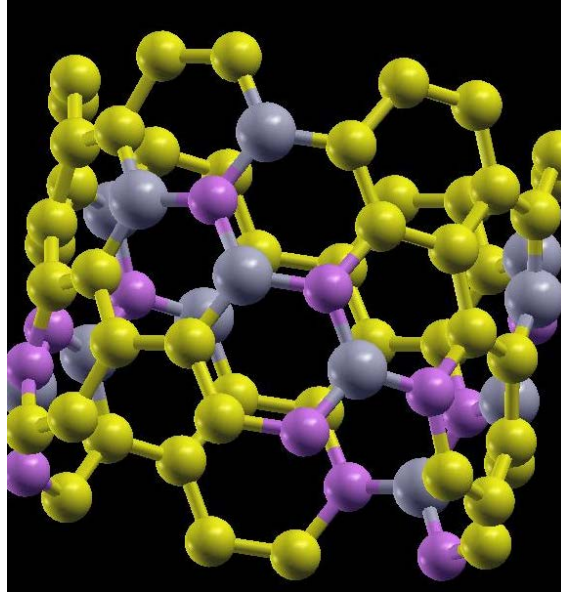


Figure 8. Relaxed structure of pristine (8,6) BC₄N nanotube, C atoms are in yellow, N atoms are in pink and B atoms are in grey

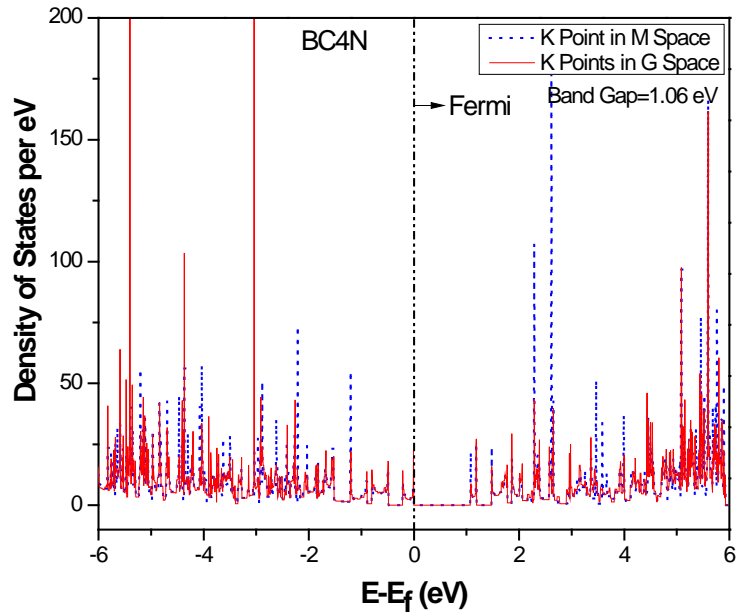


Figure 9. Total Density of States (DoS) for perfect (6,6) BC₄N nanotube, Fermi level is at zero.

3.3 Effect of Li on BNNT and BC₄N nanotube

In this section we will present the modification of structure and electronic properties of pristine BN NT and BC₄N nanotube due to formation of lithium through interaction between boron and neutron. Lithium has one *s* electron in the outer shell and is very reactive. As lithium is metallic there will be charge transfer between the tube and the lithium which will change the density of the states (DoS) of the system. The relaxed structure of BN NT substituted with Li in place of a B atom is shown in Fig. 10. We can see that the structure is severely deformed but the tubular shape is intact. Figure 11 presents the DoS for Li substituted (in place of B) BN NT. There is a drastically reduction of the band gap of BNNT due to presence of Li and the system becomes almost metallic.

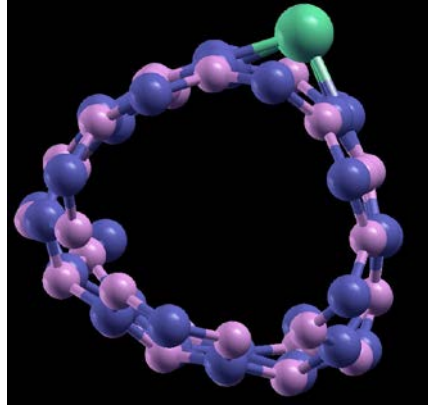


Figure 10. Relaxed structure of Li substituted (in place of B) BNNT showing severe deformation, green atom is Li and B atoms are in blue.

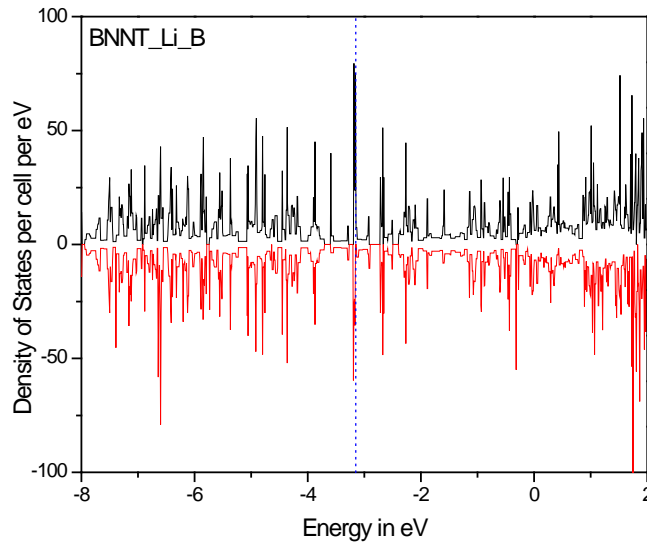


Figure 11. Total Density of States (DoS) for Li substituted (in place of B) BN NT, Fermi level is at zero

For BC_4N nanotube all the B atoms are not at the same symmetry, there are B atoms in the BN_3 ring and there are three different B atoms in the NB_3 ring. Similarly there are N and C atoms at different sites. So Li atoms can settle in any of those locations. In order to study the influence of Li atoms we have substituted Li atoms in place of B atom at the side of the NB_3 ring, at the middle of the BN_3 ring and at the connecting BN_3 - NB_3 chain. We have also studied the effect of Li as an adatom. The relaxed structure of BC_4N nanotube with Li at the side of the NB_3 ring and at the middle of the BN_3 ring is shown in the Fig. 12. The corresponding DoS plots are presented in the Fig. 13. We can notice that the tube is not deformed as in the case of Li doped BN NT. The Li atom only affects the structure in the hexagon where it is doped and in the neighbouring hexagons and the rest of the tube is not affected with the presence of Li atom. From the DoS plot in Fig. 13 we observe that for Li at the side of NB_3 ring the band reduces to 0.21 eV whereas for Li at the middle of BN_3 ring the system becomes metallic with finite DOS at the Fermi level. Figure 14 shows the relaxed structure of BC_4N with Li substituted in place of B at a position connecting NB_3 - BN_3 ring and Li as adatom. The corresponding DoS plots are presented in the Fig. 15. Here also we do not observe much structural deformation for both the cases. In both these cases the system becomes almost metallic but the structure remains almost the same.

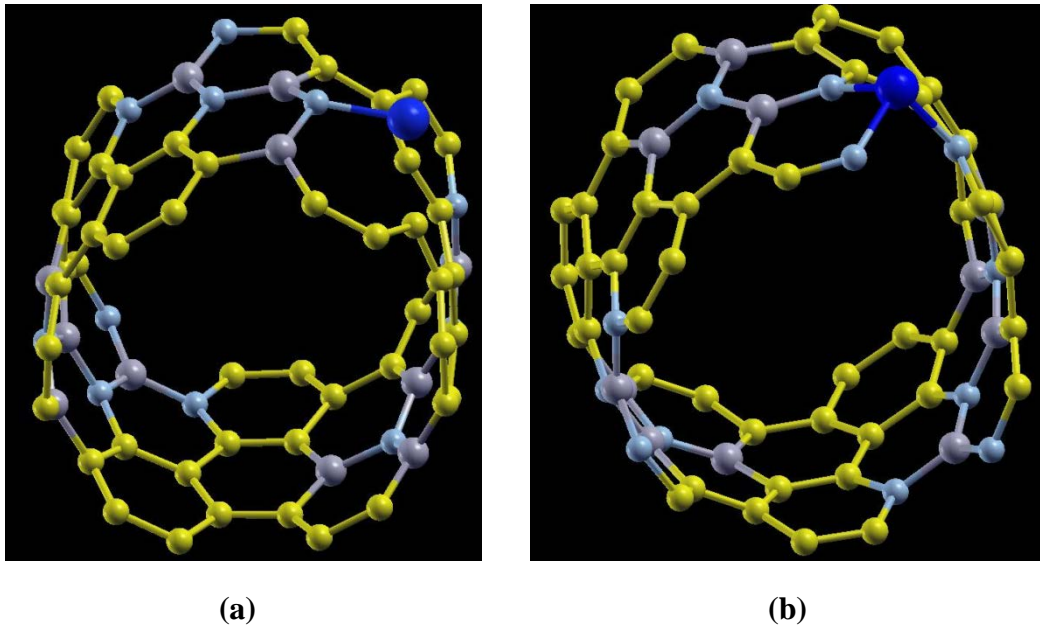


Figure 12. Relaxed structure of BC_4N with Li (a) at the side of the NB_3 ring and (b) at the middle of the BN_3 ring, blue atom is Li, C atoms are in yellow and N atoms are in cyan.

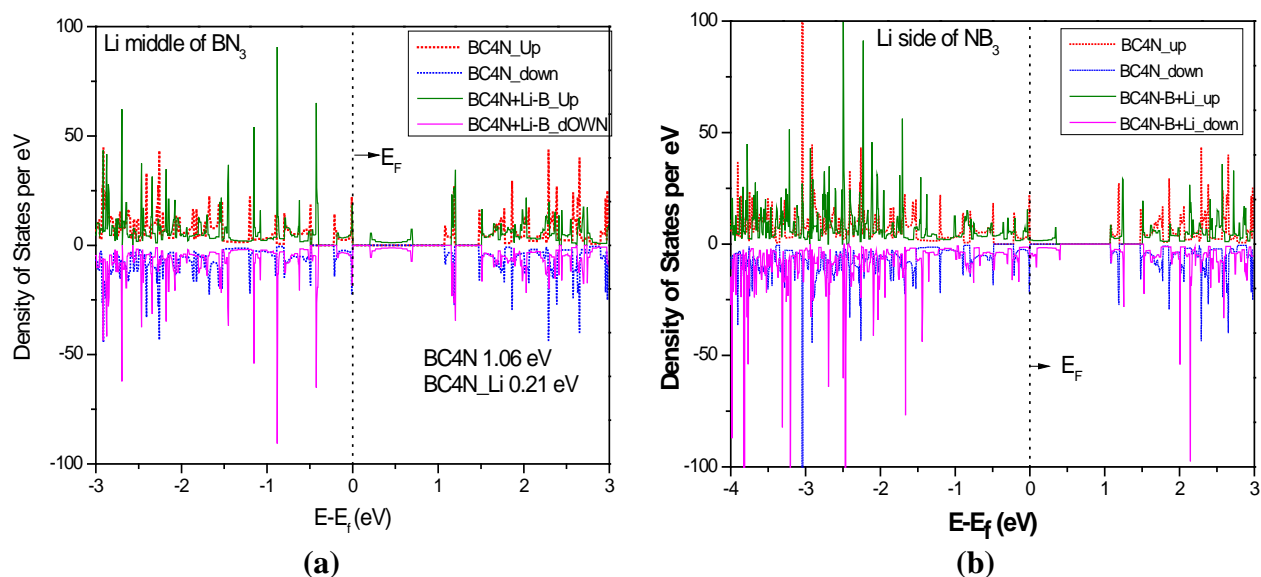


Figure 13. Total Density of States (DoS) for Li substituted (in place of B) BC₄N (a) at the side of the NB₃ ring and (b) at the middle of the BN₃ ring, Fermi level is at zero.

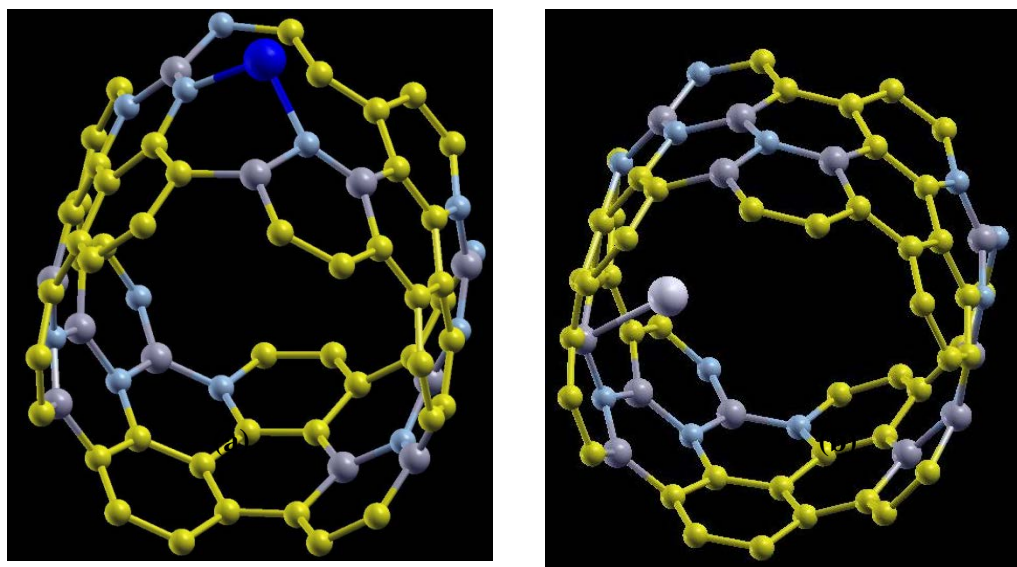


Figure 14. Relaxed structure of BC₄N with Li (a) at the connecting BN₃-NB₃ ring, blue atom is Li and (b) as an adatom down the carbon hexagon at the middle of the BN₃ ring, silver atom is Li.

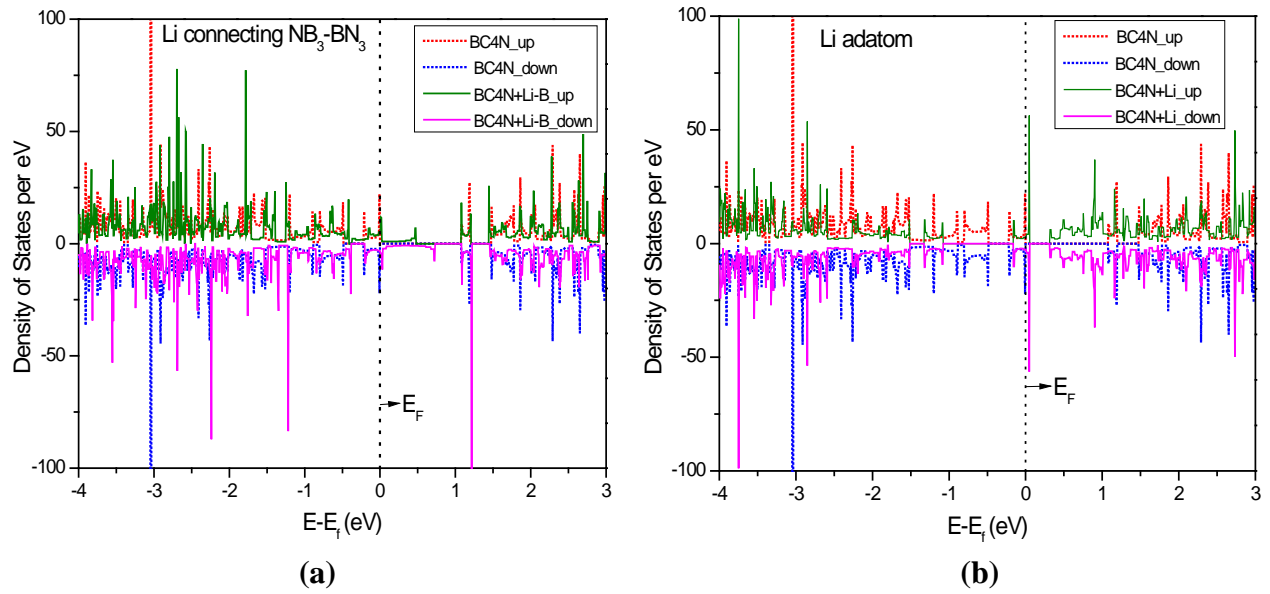


Figure 15. Total Density of States (DOS) for Li substituted (in place of B) BC₄N (a) at the connecting position of NB₃-BN₃ ring and (b) as adatom in the below C atoms, Fermi level is at zero.

3.4 Tuning the electronic properties to negate the effect of Li

We have seen in the previous sections that formation of Li alters the electronic and structural properties of both BN NT and BC₄N nanotube. As these tubes become almost metallic it is required to tune its electronic properties such that they remain as semiconductors even after the accumulation of Li. We have adopted the approach of dopinng which can potentially negate the effect of Li. Here the choice of the dopant is very crucial. As we need to move from metallic to semiconducting behaviour dopant metal atoms are obviously not suitable. The heavy element may introduce lots of deformation and the inert elements do not form strong bond with the nanotubes. So in this study we have used F, Cl and O as dopants to transform metallic behaviour of (BC₄N + Li) nanotube to semiconducting behaviour. We have considered substitutional and adatom dopants to increase the band gap of (BC₄N + Li) system. Figure 16(a) presents the DoS for F doped (BC₄N+Li) system. Here the F atom is substituted in place of one C atom whereas Li occupied the place of a B atom. It is very interesting to see that the influence of F nullifies the effect of Li and increases the band gap to around 1 eV. Thus this system (BC₄N – B + Li – C + F) seems to promising for direct conversion neutron detection. Figure 16(b) shows the DoS for F added (BC₄N – B + Li) system where F acts as an addatom to the system. Here also band gap increases up to 1 eV. It is again encouraging to notice that F negates the effect of Li and does not increase the band gap beyond the actual band gap of BC₄N. We have achieved similar results for O and Cl doped (BC₄N – B + Li) system. Figure 17(a) shows the DoS for O doped (BC₄N + Li) system. Here O atom is substituted in place of one C atom whereas Li occupies the place of a B atom. Doping of O is also able to widen the band gap to around 1 eV. Figure 17(b) presents the similar plot for Cl doping where band gap also extends up to 1 eV. In summary we have succeeded in increasing the band gap of (BC₄N + Li) system to negate the adverse effect of Li on the structural and electronic structure of boron based nanotubes.

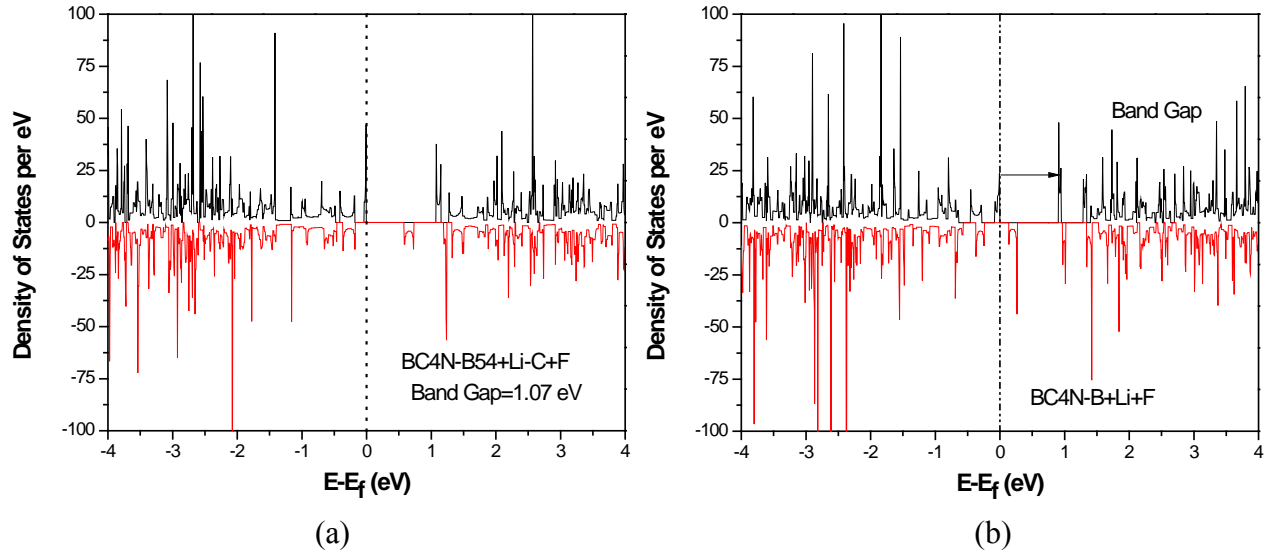


Figure 16. Total Density of States (DoS) for (a) F substituted (in place of C) in $BC_4N - B + Li$ system (b) F as adatom in $BC_4N - B + Li$ system, Fermi level is at zero.

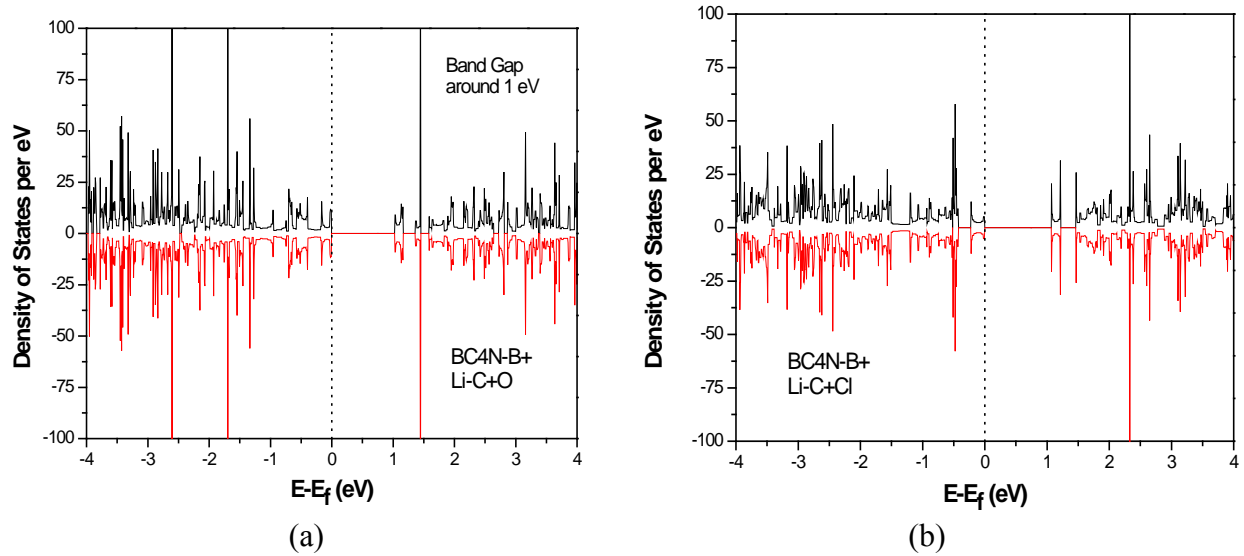


Figure 17. Total Density of States (DoS) for (a) O substituted (in place of C) in $BC_4N - B + Li$ system (b) Cl substituted (in place of C) in $BC_4N - B + Li$ system, Fermi level is at zero.

4. Summary

We have investigated the structure and electronic properties of BN and BC_4N nanotubes using density functional theory (DFT) simulations. The interaction between boron and neutron produce Li which has the potential to destabilize the structure as well as adversely affect the electronic properties. We have observed that addition of Li reduces the band gap of BNNT and BC_4N

nanotubes and makes them almost metallic. To prevent the reduction of band gap and to maintain structural integrity, we have proposed adding dopants in the nanotubes prior to irradiation with neutrons. We have successfully identified several dopants (F, O, Cl) which can retain the semiconducting and structural properties of BC₄N nanostructures.

References

1. D. Golberg et al. "Boron Nitride Nanotubes," *Adv. Mater.*, **19**, 2413–2432 (2007).
2. Y. J. Cho et al. "Electronic Structure of Si-Doped BN Nanotubes Using X-ray Photoelectron Spectroscopy and First-Principles Calculation," *Chem. Mater.*, **21**, 136 (2009).
3. Y. Miyamoto, A. Rubio, M. L. Cohen & S. G. Louie, "Chiral Tubules of Hexagonal BC₂N," *Phys. Rev. B*, **50**, 4976 (1994).
4. Xiaojun Wu & X. C. Zeng, "Adsorption of transition-metal atoms on boron nitride nanotube: A density-functional study," *Chem. Phys.* **125**, 044711 (2006).
5. Kalyan Raidongia et al., "Synthesis, Structure and Properties of Homogeneous BC₄N Nanotubes," *J. Mater. Chem.* **18**, 83 (2008).
6. G. Kresse & J. Hafner, "Ab Initio Molecular Dynamics for Liquid Metals," *Phys. Rev. B* **47**, R558 (1993).
7. G. Kresse & J. Hafner, "Ab initio Molecular-dynamics Simulation of the Liquid-metal–Amorphous-semiconductor Transition in Germanium," *Phys. Rev. B* **49**, 14251 (1994).
8. G. Kresse & J. Furthmüller, "Efficiency of Ab-initio Total Energy Calculations for Metals and Semiconductors Using a Plane-wave Basis set," *Comput. Mater. Sci.*, **6**, 15 (1996).
9. G. Kresse & J. Furthmüller, "Efficient Iterative Schemes for ab Initio Total-energy Calculations Using a Plane-wave Basis set," *Phys. Rev. B*, **54**, 11169, (1996).
10. J. P. Perdew et al., "Atoms, Molecules, Solids, and Surfaces: Applications of the Generalized Gradient Approximation for Exchange and Correlation," *Phys. Rev. B*, **46**, 6671 (1992).
11. H. J. Monkhorst & J. D. Pack, "Special Points for Brillouin-zone Integrations," *Phys. Rev. B* **13**, 5188, (1976).
12. M. Mirzaei & M. Mirzaei, "Sulfur doping at the tips of (6,0) boron nitride nanotube: A DFT study," *Physica E*, **42**, 2147 (2010).
13. J. Wu & W. Zhang, "Tuning the magnetic and transport properties of boron-nitride nanotubes via oxygen-doping," *Solid state commu.* **149**, 486 (2009).
14. X. Blase et al. "Stability and Band Gap Constancy of Boron Nitride Nanotubes," *Europhys. Lett.*, **28**, 335 (1994).
15. A. Zunger, A. Katzir, and A. Halperin, A., "Optical Properties of Hexagonal Boron. Nitride," *Physical Review B* **13** 5560 (1976).

Part II. Nanowire Sensors: Fabrication and Characterization

1. Introduction

Many applications with nanowires (NWs) as active materials in electronic devices and sensors have been developed.^{1,2} Unconventional electronics such as flexible and stretchable electronics enables novel device applications whose versatility exceeds that of the planar, rigid counterparts. Recently, semiconductor NWs have shown promising potential for the applications of flexible and stretchable electronics,³⁻¹⁰ where assembly of NWs on flexible and stretchable substrates represents a key step. The processing limitations of these unconventional substrate materials, elastomers in particular, make such device fabrication more challenging compared to conventional hard substrates.¹¹ The ability to effectively align, assemble and transfer NWs on flexible and stretchable substrates is thus of great importance. A number of methods have been developed for the assembly and alignment of NWs such as flow-assisted alignment, Langmuir-Blodgett technique, external field-assisted alignment and contact printing; interested readers are referred to recent reviews^{4,6} Though some of these methods are compatible with flexible substrates (e.g., plastics), almost none are with stretchable substrates (e.g., elastomers).

An alternative method, strain-release assembly, was recently developed for aligning semiconductor and metal NWs on elastomeric substrates (e.g., polydimethylsiloxane, PDMS).¹² This method offers a simple and effective approach to achieve highly aligned NWs with large area coverage and controlled density; the NWs could be from either as-grown substrates (e.g., Si NWs) or solution-based dispersions (e.g., Ag NWs).

In the present work, we demonstrated the utility of the strain-release assembly in fabricating functional NW devices on different unconventional substrates (e.g., stretchable and flexible substrates). A modified transfer printing process¹³⁻¹⁶ was developed which uses the alignment substrate (i.e., PDMS) itself as the “stamp” to transfer aligned NWs to other types of substrates. Three representative devices were fabricated and characterized to show applications in stretchable electronics, strain sensing and optical sensing. Integrating the strain-release method for NW alignment/assembly with the transfer printing to diverse substrates provides a simple and scalable approach for developing NW-based unconventional devices.

2. Experimental

Both Si and ZnO NWs were synthesized by the vapor-liquid-solid (VLS) method on Si/SiO₂ substrates with Au colloids as the catalysts.^{21,35} The NW diameters are determined by the size of the Au colloids; the diameters for Si and ZnO NWs are 15-60 nm and 20-80 nm, respectively. The NW lengths typically range from 5 to 30 μm . Both Si and ZnO NWs in this study are single crystalline. Si NWs grow primarily along $\langle 111 \rangle$ (though $\langle 110 \rangle$ and $\langle 112 \rangle$ directions are possible for NWs with smaller diameter); ZnO NWs grow along $\langle 0001 \rangle$ direction. Si NWs have little or no visible amorphous oxide layer on the NW surface. More details on the NW synthesis and structural characterization can be seen in the Supplementary Materials.

PDMS was prepared at 10:1 ratio of Dow Corning SYLGARD 184 elastomer and curing agent, respectively. UVO treatment of the PDMS surface was performed for 5 minutes for stretchable device fabrication. Device stretching was achieved by a custom-built mechanical testing stage

and directly observed under optical microscopy while probing via micromanipulator stage for in-situ I-V measurements.

PCL pellets were dissolved in a toluene solution and heated to 65 °C while stirring for 60 minutes to ensure a uniform solution. PET was rinsed in acetone and DI water before PCL deposition was performed via dynamic spin-coating at 1,000 RPM for a duration of 60 seconds to form a thin adhesion layer (10-30 nm thick).²² To transfer the NWs, PCL-coated PET and PDMS were pre-heated to the melting point of PCL (~65 °C), placed in contact for five minutes, and then the PDMS was peeled off to complete the process. PET bending was performed by applying compressive strain with the mechanical testing stage to induce bending. Radius of curvature was measured at the device position (chosen such that the device experienced the largest curvature under bending).

3. Results and Discussion

The as-grown NWs were transferred by contact printing¹⁷ onto a pre-strained PDMS substrate (90% pre-strain), which was then released to align the NWs in the transverse direction (Figure 1).¹² The NWs are uniformly aligned across millimeter length scales with relatively high densities (2~3 NW/ μm). These aligned NWs form the basis for subsequent device developments.

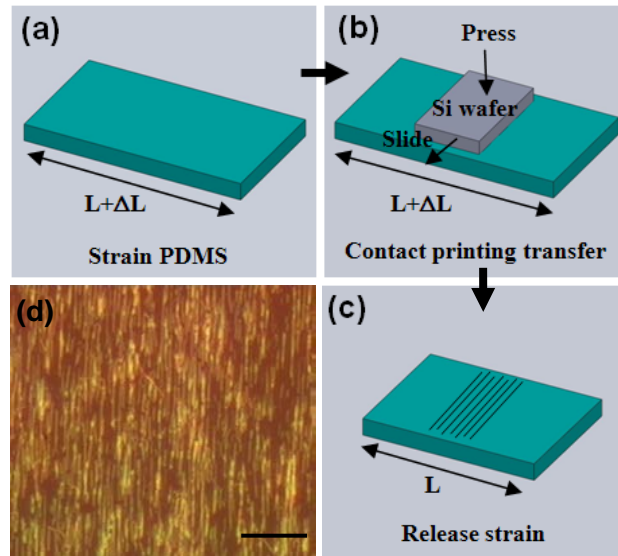


Figure 1. (a-c) Schematic of the strain-release assembly method and (d) optical image of resulting SiNWs aligned in the transverse direction on PDMS (scale bar 10 μm).

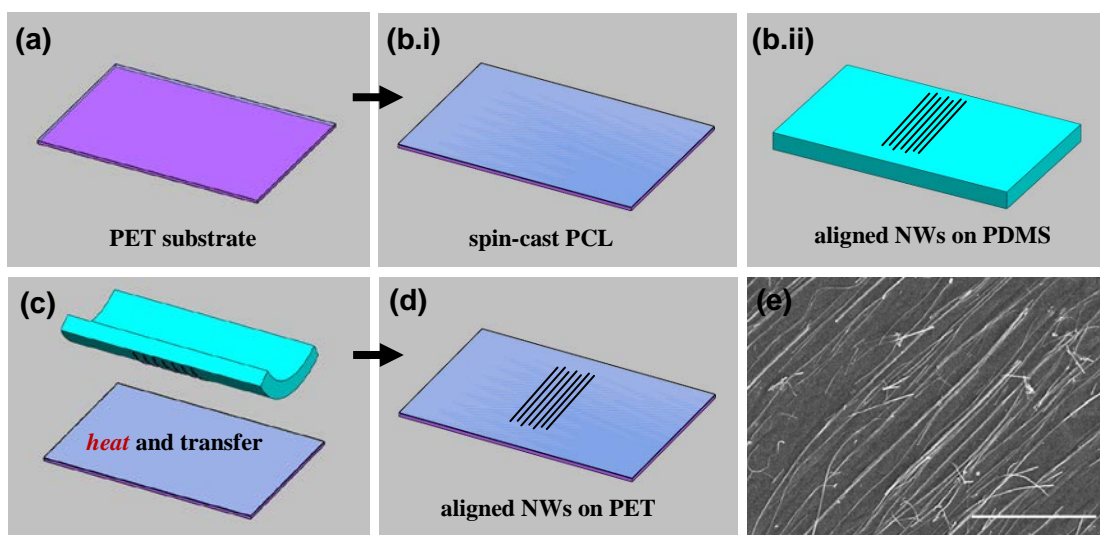


Figure 2. (a-b.i) NW transfer printing schematic including adhesion layer deposition, (b.ii) NW assembly on PDMS stamp, and (c-d) heated contact transfer printing to PET. (e) SEM image of aligned SiNWs after transfer to PET (scale bar 5 μm).

3.1 Flexible Strain Sensors

PDMS has been employed as a stamping material by which to transfer materials even devices, from a rigid, planar substrate to unconventional substrates such as plastic or glass.^{6,13,14} Since our strain-release assembly method utilizes PDMS to induce the alignment of NWs, it could be seamlessly integrated into a similar transfer printing process. This would enable the use of other materials as the final substrate, greatly expanding the versatility of the strain-release assembly method for device fabrication. To demonstrate the feasibility of using the alignment process in conjunction with the PDMS stamping, we have fabricated NW devices on a flexible plastic – polyethylene terephthalate (PET) – substrate.

The PET substrate was coated with a thin layer of polycaprolactone (PCL) by spin-coating a PCL-toluene solution on the PET surface (Figure 2). The PCL served as an adhesion layer to promote the transfer of NWs from the PDMS to the plastic.²² SiNWs were aligned separately on PDMS via the strain-release method with 90% pre-strain as described above (Figure 2b.ii). The NWs were then transferred to the PET by a heated contact printing process (Figure 2c-d). Approximately 85% of the NWs were transferred to the plastic substrate by this process after transfer to the PET, as seen in Figure 2e. Titanium electrodes, forming Schottky-contact with Si,²³ were deposited using the same process above to fabricate SiNW array devices on PET; the NWs were aligned in the longitudinal direction with respect to the applied load. The same shadow mask was used, so the same device size (25 by 25 μm electrodes and 10 μm wide gap) was obtained. The electrical performance (i.e., I - V characteristic) of a device under bending was measured as the two clamped ends of the substrate were brought closer together by the Fullam mechanical testing stage in the probe station (Figure 3a). The device was able to bend to a small radius (4 mm). The resistance increased with increasing curvature and the strain in the NW can

be calculated from the radius of curvature using classic beam bending mechanics (Figure 3b). The maximum strain in the NW was $\sim 1.6\%$, well below the fracture strain of the 20-50 nm diameter SiNWs as previously reported by our group,²¹ indicating a reliable device able to bend to small radii without failure. The sensitivity of the device was measured by the gauge factor GF,

$$GF = \frac{\Delta R}{R} \varepsilon^{-1} \quad (5)$$

where R is the resistance, and ε is the mechanical strain. Our strain sensor device exhibited very large gauge factors (from 300 to >1000) depending on the strain level, which far exceeds that of conventional metal strain gauges and compares well with other NW-based strain sensors.^{14,24,25}

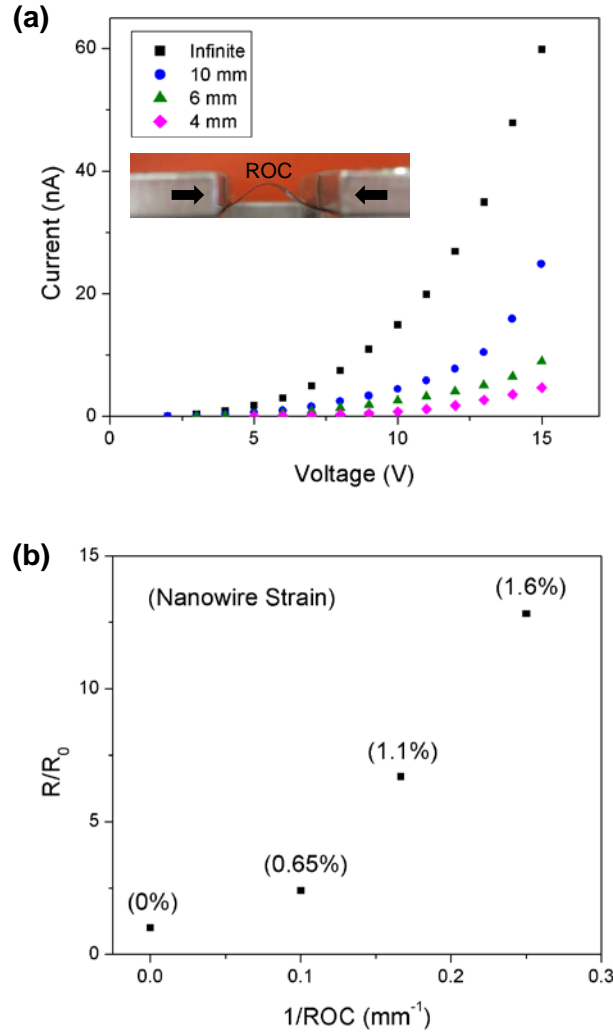


Figure 3. (a) I-V performance of SiNW device on PET under bending. Inset image is of custom mechanical stage used during bending experiments with radius of curvature (ROC) location indicated. (b) Resistance change and NW tensile strain with respect to ROC.

3.2 Flexible UV Sensors

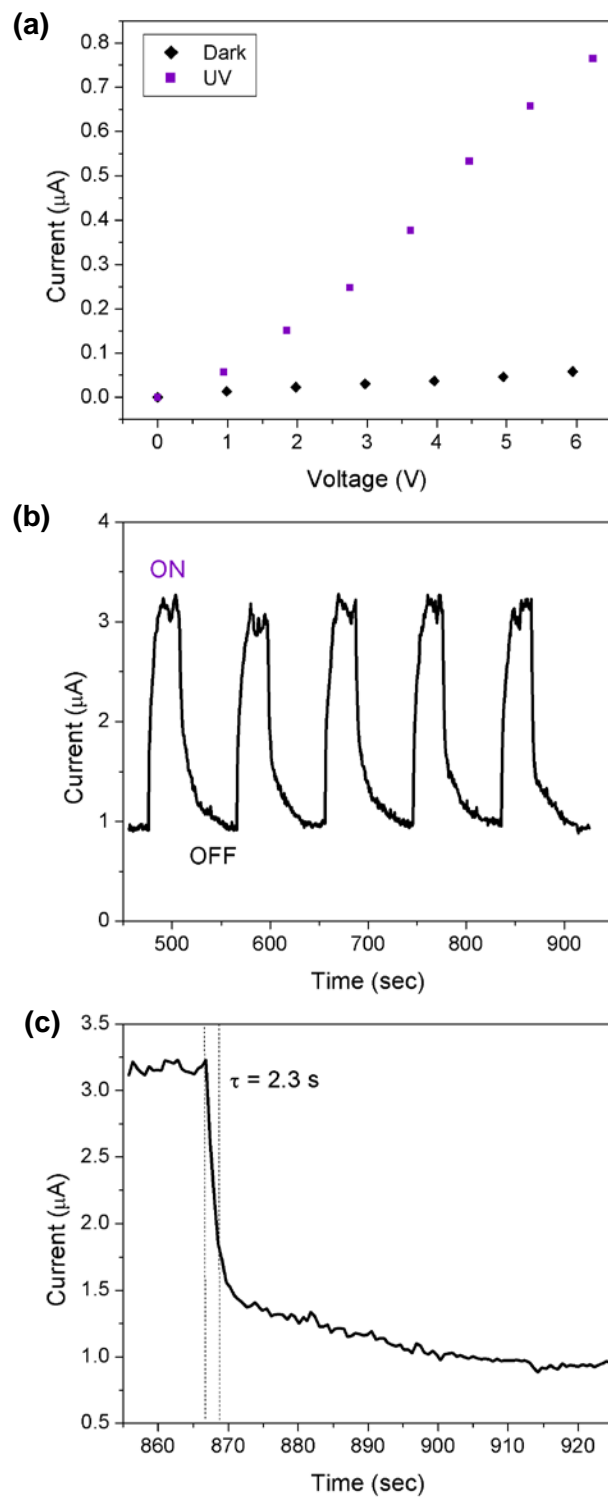


Figure 4. (a) Dark (off) vs. photoresponse (on) I-V measurements of ZnO NW UV sensor. (b) Sensor photocurrent response to cyclic UV illumination in air at a bias of 20 V. (c) Recovery response of the NW sensor

Zinc oxide (ZnO) NW UV sensors were fabricated similarly on plastic by the strain-release assembly method in conjunction with the PDMS transfer printing process to a PCL-coated PET substrate. The ZnO NWs were also aligned with 90% PDMS pre-strain. Titanium electrodes, forming ohmic contacts with ZnO,^{26,27} were deposited to fabricate two-terminal ZnO NW devices on flexible plastic. Under UV exposure (BHK Analamp Mercury lamp, $\sim 30 \mu\text{W cm}^{-2}$ for 365 nm at a distance of 20 cm from the lamp), the resistances of the ZnO NWs decreased significantly, allowing for sensitive detection of light in the UV range. The dark I-V characteristics along with UV illumination response for one such single-NW device are shown in Figure 4a. This response is due to the presence of adsorbed oxygen molecules on the NW surfaces, which are desorbed by recombination with holes on the surface after photo-induced electron-hole pair generation inside the NW.^{28, 29} The unpaired electrons left behind directly lead to a measurable increase in current under an applied bias.

Cycling the UV lamp on and off resulted in repeatable sensor response and recovery from the NW device (Figure 4b). On-off cycles were performed at a 1 to 2 time ratio to allow for sufficient device recovery between cycles. UV photocurrent response on-off ratios ranged from approximately 3.5:1 to 15:1 for our devices, lower than that of other reported ohmic devices (>100)²⁸⁻³², which might be due to a low-intensity UV source and/or small NW diameter used in our devices (20-80 nm compared to 200 nm and 150-300 nm as previously reported^{28,32}). The recovery time of the sensor, defined as the time for current to decrease to $1/e$ (37%) of the on-current after the lamp has been switched off, was found to be as fast as ~ 2.3 seconds (Figure 5c). This recovery time is quicker than similar ohmic contact ZnO NW UV sensors previously reported²⁸, which can also be attributed to the smaller NW diameters used in our devices. It was shown that smaller ZnO NW diameters exhibited faster recovery times.²⁸ Comparing our ZnO NW UV sensor with other similar UV sensors indicates a benefit of our device in its fast recovery, making it suitable for fast sensing operation where very large photocurrent gain is not required. Our sensors demonstrated potential for optical sensing and switching device applications on flexible substrates.

4. Summary

We have demonstrated the fabrication of three types of NW devices using the strain-release assembly method that enables transference to unconventional substrates when combined with transfer printing. The devices address a range of potential applications: 1) a stretchable SiNW device that is built on the new concept of transverse buckling exhibits constant performance across a large strain range with applications in stretchable electronics; 2) a flexible SiNW strain sensor shows very large gauge factor; 3) a flexible ZnO NW UV sensor shows reliable photo-response and fast recovery for optoelectronic sensing and switching applications. The demonstrated fabrication process can be readily applied to other one-dimensional nanostructures such as carbon nanotubes.^{33,34} The results herein exemplify the versatility of our assembly process through realization of various functional device types on unconventional substrates in a simple, scalable and effective manner.

References

- (1) Lu, W.; Lieber, C. M. *J. Phys. D.: Appl. Phys.* **2006**, *39*, R387–R406.
- (2) Xia, Y.; Yang, P.; Sun, Y.; Wu, Y.; Mayers, B.; Gates, B.; Yin, Y.; Kim, F.; Yan, H. *Adv. Mater.* **2003**, *15*, 353–389.
- (3) McAlpine, M. C.; Ahmad, H.; Wang, D.; Heath, J. R. *Nat. Mater.* **2007**, *6*, 379–384.
- (4) Fan, Z.; Ho, J. C.; Takahashi, T.; Yerushalmi, R.; Takei, K.; Ford, A. C.; Chueh, Y.-L.; Javey, A. *Adv. Mater.* **2009**, *21*, 3730–3743.
- (5) Xu, F.; Lu, W.; Zhu, Y. *ACS Nano* **2010**, *5*, 672–678.
- (6) Liu, X.; Long, Y.-Z.; Liao, L.; Duan, X.; Fan, Z. *ACS Nano* **2012**, *6*, 1888–1900.
- (7) Duan, X. *MRS Bull.* **2007**, *32*, 134–141.
- (8) Takei, K.; Takahashi, T.; Ho, J. C.; Ko, H.; Gillies, A. G.; Leu, P. W.; Fearing, R. S.; Javey, A. *Nat. Mater.* **2010**, *9*, 821–826.
- (9) Javey, A.; Nam, S.; Friedman, R. S.; Yan, H.; Lieber, C. M. *Nano Lett.* **2007**, *7*, 773–777.
- (10) Ryu, S. Y.; Xiao, J.; Park, W. I.; Son, K. S.; Huang, Y. Y.; Paik, U.; Rogers, J. A. *Nano Lett.* **2009**, *9*, 3214–3219.
- (11) Lee, J.; Park, C.; Whitesides, G. *Anal. Chem.* **2003**, *75*, 6544–6554.
- (12) Xu, F.; Durham, J. W.; Wiley, B. J.; Zhu, Y. *ACS Nano* **2011**, *5*, 1556–1563.
- (13) Sun, Y.; Rogers, J. A. *Nano Lett.* **2004**, *4*, 1953–1959.
- (14) Lee, C. H.; Kim, D. R.; Zheng, X. *PNAS* **2010**, *107*, 9950–9955.
- (15) Hsieh, G.-W.; Wang, J.; Ogata, K.; Robertson, J.; Hofmann, S.; Milne, W. I. *J. Phys. Chem. C* **2012**, *116*, 7118–7125.
- (16) Madaria, A.; Kumar, A.; Ishikawa, F.; Zhou, C. *Nano Res.* **2010**, *3*, 564–573.
- (17) Fan, Z.; Ho, J. C.; Jacobson, Z. A.; Yerushalmi, R.; Alley, R. L.; Razavi, H.; Javey, A. *Nano Lett.* **2008**, *8*, 20–25.
- (18) Rogers, J. A.; Someya, T.; Huang, Y. *Science* **2010**, *327*, 1603–1607.
- (19) Qin, Q.; Zhu, Y. *ACS Nano* **2011**, *5*, 7404–7410.
- (20) Lacour, S.; Jones, J.; Wagner, S.; Li, T.; Suo, Z. *Proc. IEEE* **2005**, *93*, 1459–1467.
- (21) Zhu, Y.; Xu, F.; Qin, Q.; Fung, W. Y.; Lu, W. *Nano Lett.* **2009**, *9*, 3934–3939.
- (22) Hyun, D. C.; Moon, G. D.; Cho, E. C.; Jeong, U. *Adv. Funct. Mater.* **2009**, *19*, 2155–2162.
- (23) Motayed, A.; Bonevich, J. E.; Krylyuk, S.; Davydov, A. V.; Aluri, G.; Rao, M. V. *Nanotechnology* **2011**, *22*, 075206.
- (24) He, R.; Yang, P. *Nat. Nanotechnol.* **2006**, *1*, 42–46.
- (25) Zhou, J.; Gu, Y.; Fei, P.; Mai, W.; Gao, Y.; Yang, R.; Bao, G.; Wang, Z. L. *Nano Lett.* **2008**, *8*, 3035–3040.
- (26) Kim, S.; Jang, H.; Kim, J.; Jeon, C.; Park, W.; Yi, G.; Lee, J. *J. Electron. Mater.* **2002**, *31*, 868–871.
- (27) Chang, P.-C.; Fan, Z.; Chien, C.-J.; Stichtenoth, D.; Ronning, C.; Lu, J. G. *Appl. Phys. Lett.* **2006**, *89*, 133113.
- (28) Soci, C.; Zhang, A.; Xiang, B.; Dayeh, S. A.; Aplin, D. P. R.; Park, J.; Bao, X. Y.; Lo, Y. H.; Wang, D. *Nano Lett.* **2007**, *7*, 1003–1009.
- (29) Liu, B.; Wang, Z.; Dong, Y.; Zhu, Y.; Gong, Y.; Ran, S.; Liu, Z.; Xu, J.; Xie, Z.; Chen, D.; Shen, G. *J. Mater. Chem.* **2012**, *22*, 9379–9384.
- (30) Kind, H.; Yan, H.; Messer, B.; Law, M.; Yang, P. *Adv. Mater.* **2002**, *14*, 158–160.
- (31) Wu, W.; Bai, S.; Cui, N.; Ma, F.; Wei, Z.; Qin, Y.; Xie, E. *Sci. Adv. Mater.* **2010**, *2*, 402–406.

- (32) Yang, Q.; Guo, X.; Wang, W.; Zhang, Y.; Xu, S.; Lien, D. H.; Wang, Z. L. *ACS Nano* **2010**, *4*, 6285–6291.
- (33) Engel, M.; Small, J. P.; Steiner, M.; Freitag, M.; Green, A. A.; Hersam, M. C.; Avouris, P. *ACS Nano* **2008**, *2*, 2445–2452.
- (34) Zhu, Y.; Xu, F. *Adv. Mater.* **2012**, *24*, 1073–1077.
- (35) Xu, F.; Qin, Q.; Mishra, A.; Gu, Y.; Zhu, Y. *Nano Res.* **2010**, *3*, 271–280.

Part III. Irradiation Response of BN Nanotubes using Molecular Dynamics (MD) Simulations

Introduction

Due to the recent and elevated threat of the spread of nuclear materials across international borders, there is a renewed interest in the use of advanced radiation detection technologies for homeland security and national defense applications. As a result, there is a greater emphasis on the development of more efficient, next-generation neutron-detection materials. Since neutrons are electrically neutral, solid-state detection requires a capture reaction followed by the generation of electron-hole pairs that can be separated, collected, and eventually transduced into a low-voltage, detectable electrical signal [1, 2].

Solid-state devices can be broken into two classes: direct and indirect conversion. Detection with indirect conversion involves two distinct materials – a neutron sensitive material for capture reactions (such as boron) and a semiconducting material for electron–hole pair generation (such as silicon). Advancements in the recent years have focused on optimization of indirect conversion geometries, transport and modern processing techniques for conventional semiconductors such as silicon and germanium [1]. In contrast, neutron capture and charge generation are facilitated by the same material in a direct conversion neutron detector.

Traditional choices for the detector materials such as B_5C , and uranium and gadolinium rich materials are not optimal for neutron capture, as well as generation, separation and collection of charge carriers. The limiting factor thus far originates from the rather poor semiconducting properties of direct conversion materials.

Boron nitride nanotubes

Functionalized nanostructures provide an exciting alternative where the electronic properties can be enhanced by several orders in magnitude through appropriate doping while maximizing the neutron capture reactions. One of the nanostructured materials which is relevant to neutron detection is the boron nitride nanotube (BNNT) which has several interesting properties including high neutron capture cross–section, thermal conductivity and stability, mechanical properties and chemical inertness [3,4]. Our work explores BNNTs as a direct conversion detector material that can potentially improve the spatial, temporal and energy resolution of neutron detectors. BNNTs, successfully synthesized in 1995, are the structural analogues of more

commonly encountered carbon nanotubes (CNTs). Neutron interactions however, can damage the structure of the nanotubes and can potentially decrease the efficacy of the semiconducting properties. The purpose of this study therefore, is to determine the physical response of BNNTs subject to neutron irradiation, and investigate the displacement evolution with molecular dynamics (MD) simulations.

Molecular dynamics simulations

A classical molecular dynamics (MD) approach is utilized to simulate displacement cascades in BNNTs sandwiched between two bulk (cubic) boron nitride substrates as shown in Figure 1. Classical MD simulations provide a tractable computational approach for predicting the dynamic response of materials to irradiation and have been successfully employed in the past to investigate several nuclear structural materials [5].

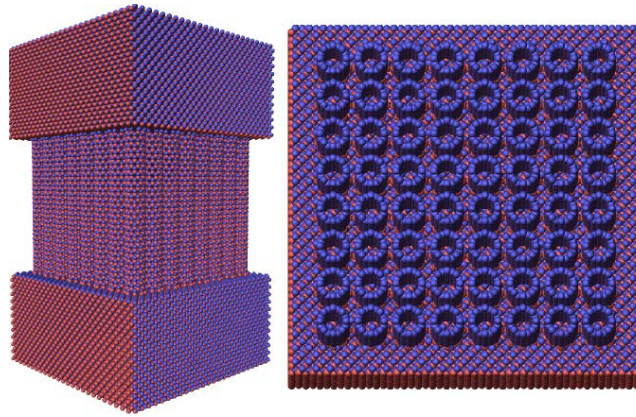


Figure 2. BNNT sandwich configuration. An 8 x 8 array of nanotubes is stabilized by c-BN substrates with an interfacial distance of 1 Å. Note that the above geometry is not optimized for field tests.

The structure consists of 64 single-walled, zig-zag (8,0) BNNTs with a radius of 3.15Å, length of 65.5Å, and center-to-center separation distance of 9.8Å. Both ends of the tubes are attached to a 42.6Å-thick cubic BN substrate, which serves to effectively stabilize the nanotube structure and dissipate heat from the displacement cascades. Each nanotube and BN substrate has 480 and 60,000 atoms, respectively.

The MD system consists of a total of 150,720 boron and nitrogen atoms whose bonds and interactions are described by a three-body Tersoff potential combined with a Ziegler-Biersack-Littmark (ZBL) universal screening function which accounts for the electrostatic repulsion at very close distances. The Tersoff interatomic potential parameters are taken from Sekkal *et al.* [6], who accurately benchmarked several key properties of bulk BN. In particular, using this optimized Tersoff potential, MD simulations resulted in a lattice constant of 3.623\AA , bulk modulus of 3.653 Mbar, and cohesive energy of 6.718 eV/atom which are in excellent agreement with the reported experimental data (3.615\AA [7], 3.69 Mbar [8], and 6.68 eV/atom [9]).

LAMMPS MD code package, developed at Sandia National Laboratories [10], is used to perform the radiation damage analysis. The system is first brought to its lowest potential energy by a constrained conjugate gradient relaxation that also ensures a zero system pressure. The radiation impact is then simulated by imparting additional kinetic energy to the primary knock-on atom (PKA) located at the center of the nanotube sandwich configuration with the additional momentum directed along a particular direction (see Fig. 2).

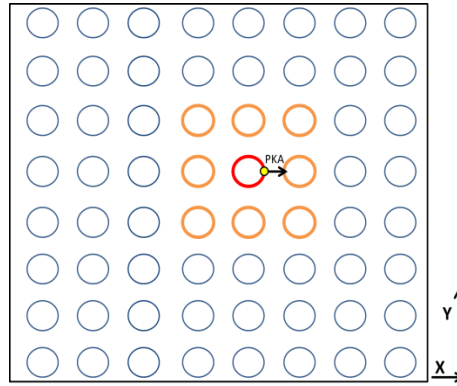


Figure 2. PKA location and direction. The red indicates the knocked tube, while orange signifies the surrounding tubes.

To dissipate the thermal energy generated during the radiation damage event and to prevent the shock waves from reentering the nanotubes, the temperature of each substrate is maintained at 300K by a Nose-Hoover thermostat. Some of the nanotube atoms are susceptible to being completely displaced from their lattice sites and travel outside of the system boundaries. If

periodic boundary conditions are used, these atoms can re-enter the simulation box and result in non-physical response. Therefore, “shrink-wrapped” boundaries are enforced to accommodate all the atoms that travel outside the original dimensions of the BNNT sandwich structure.

Statistical averaging using the iso-configurational ensemble

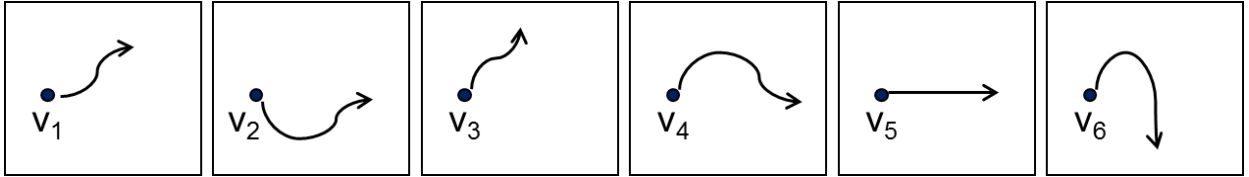


Figure 3. Iso-configurational ensemble. Several identical, NPT-equilibrated copies of the BNNT configuration are initialized with different random momenta.

In an iso-configurational ensemble (see Fig. 3), atomic displacements of each atom are averaged over several ensembles thus providing a *statistically reliable displacement metric for each atom*. The iso-configuration displacement at a particular time t is calculated as:

$$\Delta w_i(t) = \frac{1}{M} \sum_{k=1}^M [w_i^k(t) - w_i(0)] \quad (1)$$

In this equation, Δw and M signify the displacement in any of the three directions and number of ensemble copies, respectively. Note that the initial position of each atom i in the system is identical in all copies of the iso-configurational ensemble.

First we have computed the magnitude of displacement as a function of time for the fastest ten atoms in the knocked tube; the displacements are shown in Fig. 4.

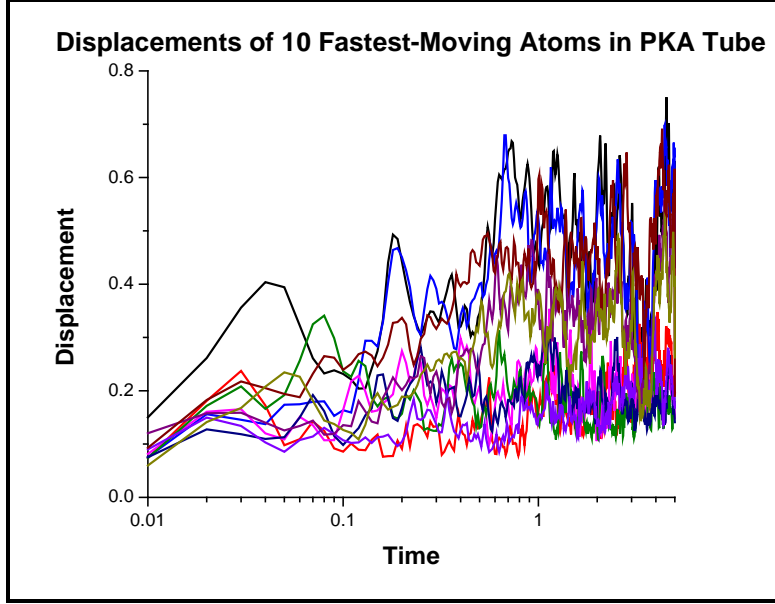


Figure 4. Displacements of the most energetic atoms in the knocked tube.

Initially, as atoms are knocked from their lattice sites, they bounce around within the tube bundle. Specifically, some atoms simply remain trapped *inside* tubes, while others bounce *between* tubes. As evident from Figure 8, displacements are gradually increasing up to 0.1 ps. Between 0.1 and 1 ps, atomic displacements begin to slowly fluctuate. Finally, after 1 ps, displacements are fluctuating very rapidly which indicates that atoms are experiencing more and more collisions as they bounce around within the array of nanotubes.

Dynamic Recovery And Fluctuations

We have constructed a probability distribution function of the per-atom displacements in the direction of the PKA energy (see Fig. 5). The distribution of displacements reflects the displacement spike and subsequent annealing of defects.

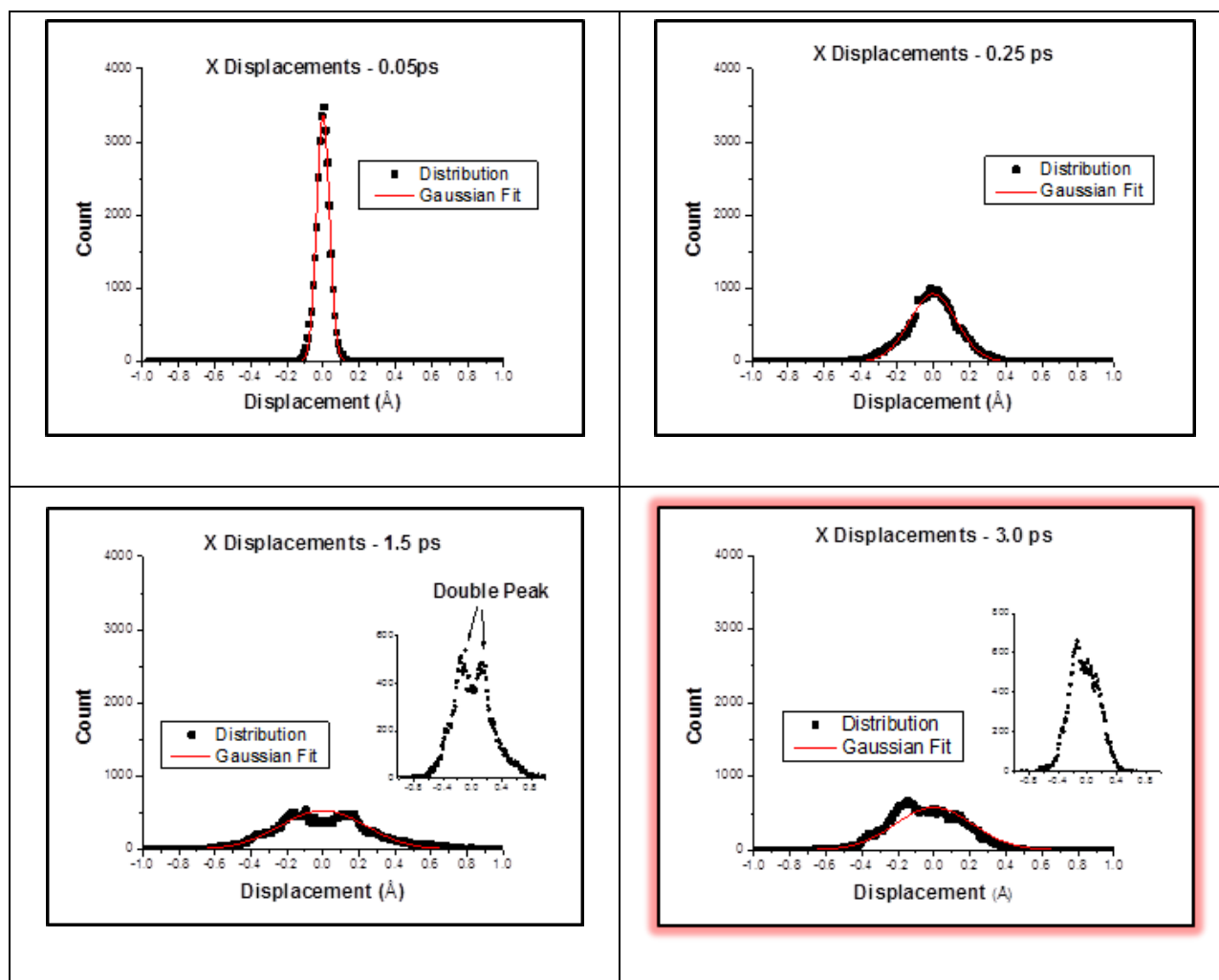


Figure 5. Coordinated motion and recovery

Immediately after the primary knock-on atom is displaced from its lattice position (0.05 ps), the distribution is narrow and Gaussian-like, as the majority of atoms are still vibrating around their equilibrium positions (see Fig. 5). As the cascade proceeds, we observe an increase in displacements and a flattening of the distribution. At 1.5 ps, a double peak occurs in the distribution, indicating that groups of atoms are moving in a coordinated fashion. This indicates that the nanotubes are moving together while dissipating the energy generated during the radiation cascade.

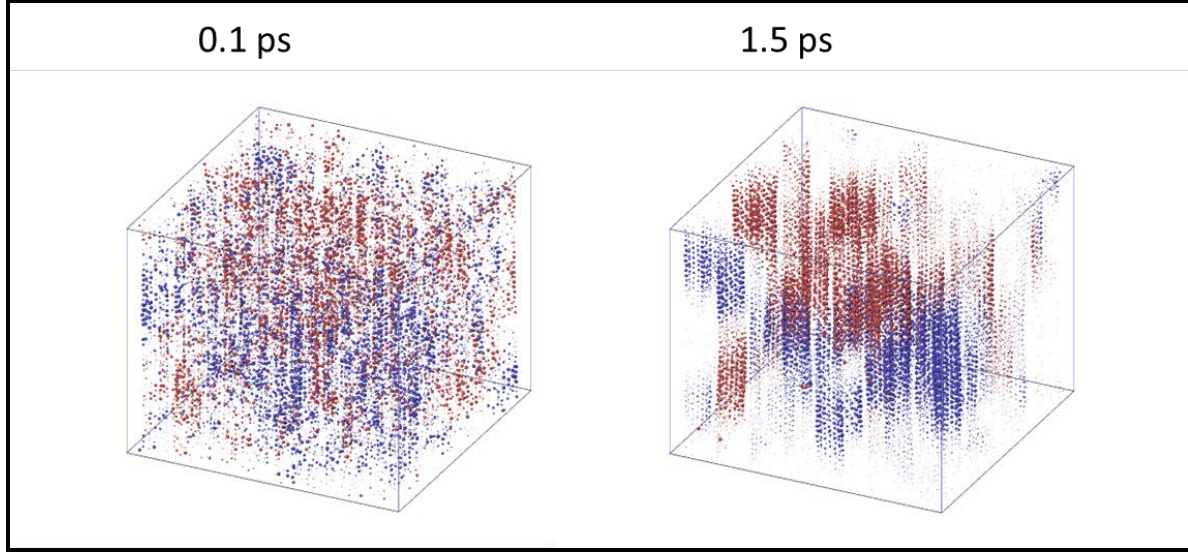


Figure 6. Visualization of displacements in the knock direction. Atoms with positive displacements are colored red, while negative displacements are blue.

Figure 6 shows a visualization of the atomic displacements in which initial positions remain the same, while the radius of each sphere changes according to the magnitude of displacement. In addition, color coding is utilized to portray positive (red) and negative (blue) displacements. Initially, positive and negative displacements are uniform throughout the volume. After the knock, we begin to see distinct and separate regions of positive and negative displacements (at 1.5 ps) indicating that tubes are moving together in a concerted manner.

Spatial Correlation Function And Correlated Dynamics

To quantify the correlated movement, we introduce the spatial correlation function, originally designed to investigate dynamic heterogeneities in glass-forming liquids. The spatial correlation function can be calculated as follows:

$$C_d(r, t) = \frac{\langle \delta x(i, t) \delta x(j, t) \rangle}{\langle [\delta x(t)]^2 \rangle} \quad (2)$$

$$\langle [\delta x(t)]^2 \rangle = \frac{1}{N} \sum_{i=1}^N [\delta x(i, t)]^2 \quad (3)$$

$$\delta x(i, t) = x(i, t) - \langle x(t) \rangle \quad (4)$$

$$\langle x(t) \rangle = \frac{1}{N} \sum_{i=1}^N x(i, t) \quad (5)$$

In the above equations, $x(i, t)$ signifies the propensity of an atom i at time t , while N represents the total number of atoms. The dynamic propensity of an atom at a particular time t is calculated as:

$$\langle r_i^2 \rangle_{IC}(t) = \frac{1}{M} \sum_{k=1}^M r^2(i, k, t) \quad (6)$$

In this equation, r^2 and M signify the dynamic propensity and number of isoconfigurational ensemble copies, respectively. Basically, the spatial correlation function, C_d , measures the average spatial correlation in the fluctuation of the propensity (at time t) from its mean value, for particles separated by a distance r in the initial configuration. To quantify the correlated movement between nanotube atoms, several tubes in the vicinity of the primary knock-on atom are divided into different segments, and the spatial correlation between different segments is computed. Below is a snapshot of 5 nanotubes where each color represents a different segment. In Figure 7, Segment 1 is located near the bottom of the nanotubes (red), while Segment 5 is at the top of the bundle (yellow).

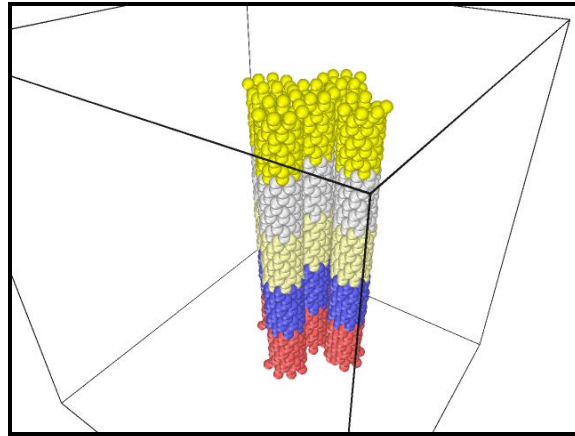


Figure 7. BNNT bundle near the PKA divided into 5 segments.

The value of C_d at different times is plotted in Fig. 8.

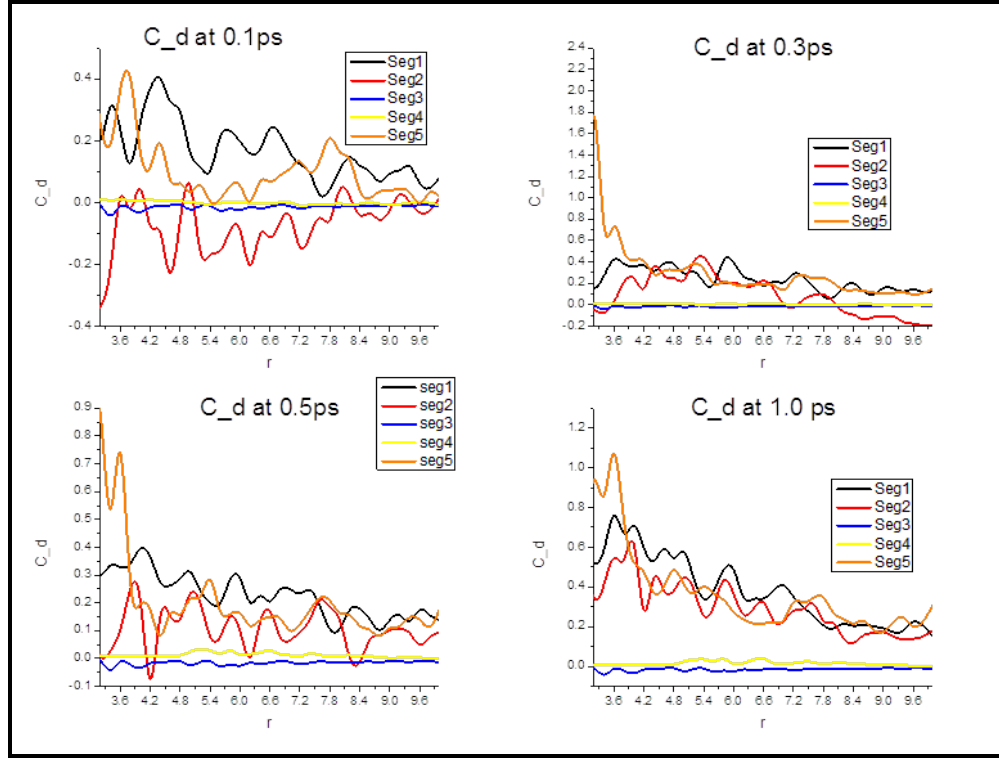


Figure 8. Spatial correlation function in different nanotube segments following knock.

From Figure 8, it can be seen that the magnitude of C_d is the greatest in segments 1 and 5, which are adjacent to the substrate interface. Segment 3, near the center of the nanotube bundle, shows little to no correlation, as atomic displacements are large and random near the PKA impact. In addition, several peaks can be observed in the plots of the spatial correlation at different values of r . For this reason, we will now compare the spatial correlation function in different segments for fixed values of r .

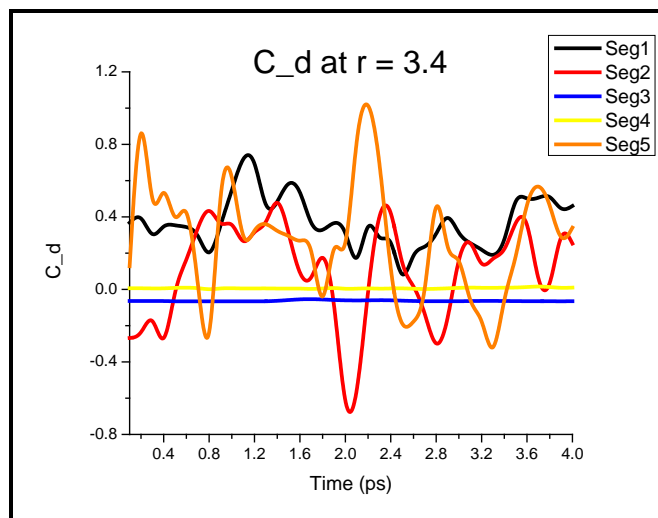


Figure 9. Spatial correlation function at $r = 3.4 \text{ \AA}$.

At a separation distance of 3.4 \AA (the tube-to-tube separation distance), we observe highly correlated movement near the substrate interface, as well as little or no correlation near the primary knock-on atom, located near the center of the BNNT bundle. Also, starting from the bottom segment (1), there is a clear trend of decreasing correlation moving towards the center of the tube.

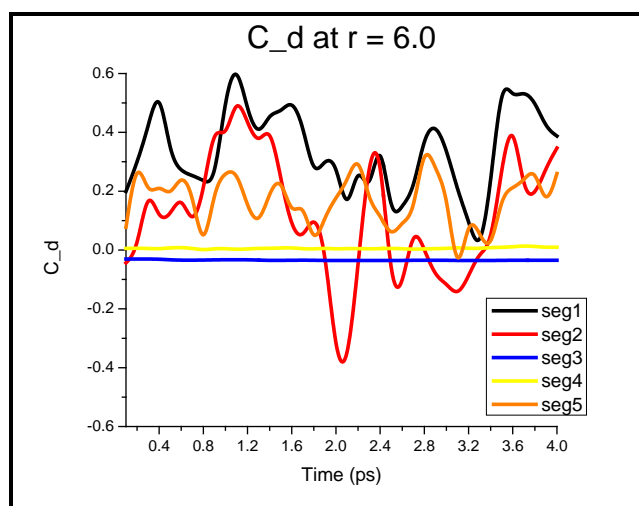


Figure 10. Spatial correlation function at $r = 6.0 \text{ \AA}$.

Similar behavior can be seen at a separation distance of 6 Å. Figure 10 clearly shows correlated movement between different segments, with large values of spatial correlation near the substrate interfaces. To illustrate the idea of *dynamic cooperation* further, snapshots of the evolution of dynamic propensities are depicted in Figure 11 (the atomic radii is based on the magnitude of the propensity, while color coding is used to indicate regions of highly mobile/immobile atoms).

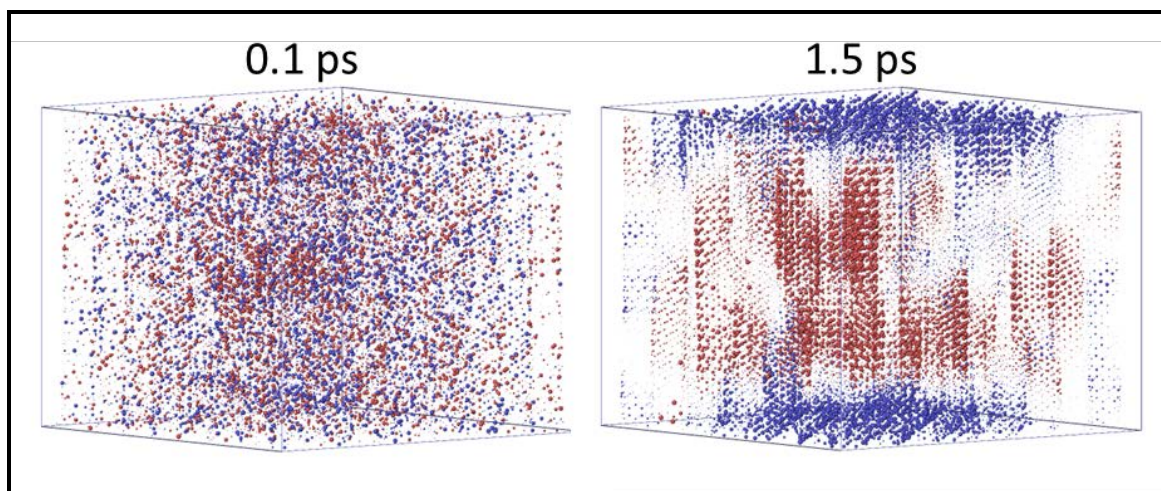


Figure 3. Visualization of the dynamic propensity of the BNNT bundle during damage cascade. Areas of red indicate highly mobile atoms, while less mobile atoms are colored blue.

As a result of the knock, a region of highly mobile atoms develops near the center of the simulation domain. Different tubes appear to be moving in a synchronized manner. In the vicinity of the substrate interface, regions of less mobile atoms (blue) develop during the cascade process. Since the two substrates effectively constrain the nanotube bundle, this behavior is expected at the interface.

Figure 12 shows the damaged region surrounding the PKA. As evident from this snapshot, significant annealing has taken place within 5 ps with very few atoms in the free space that surrounds the nanotubes.

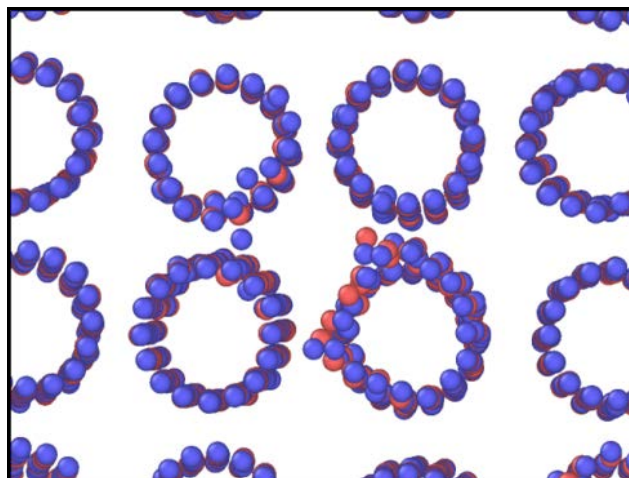


Figure 12. Irradiated BNNT structure at 5 ps showing the displacements in the transverse plane (X and Y).

The MD simulations show that the large volume of vacant space does not appear to damage the nanotubes significantly with knock energies that are $O(1)$ keV. We attribute the relatively fast recombinations, even in the presence of significant free space between the nanotubes, to the strong covalent potential between the atoms.

References

1. A. N. CARUSO, "The Physics of Solid-State Neutron Detector Materials and Geometries", *J. Phys.: Condens. Matter*, **22**, 443201 (2010).
2. B. D. MILBRATH, M. BLISS and W. J. WEBSTER, "Radiation Detector Materials: An Overview", *J. Mater. Res.*, **23**, 2561-81 (2008).
3. D. GOLDBERG, Y. BANDO, C. TANG and C. ZHI, "Boron Nitride Nanotubes", *Advanced Materials*, **19**, 2413-2432 (2007).
4. D. GOLDBERG, Y. BANDO, C. TANG and C. ZHI, "Boron Nitride Nanotubes and Nanosheets", *ACS Nano*, **4**, 2979-2993, (2010).
5. R. E. STOLLER, "Primary Radiation Damage Formation", in *Comprehensive Nuclear Materials*, (ed) R. J. M. KONINGS, Elsevier (2012).
6. W. SEKKAL, B. BOUHAFS, H. AOURAG and M. CERTIER, "Molecular-Dynamics Simulation of Structural and Thermodynamic Properties of Boron Nitride", *J. Phys.: Condens. Matter*, **10**, 4975-4984, (1998).
7. J. H. EDGAR (ed.), *Properties of Group III Nitrides (Electronic Materials Information Service (EMIS) Data Review Series*, The Institution of Electrical Engineers, London, (1994).

8. R. M. WENTZCOVITCH, M. L. COHEN and P. K. LAM, "Theoretical Study of BN, BP, and BAs at High Pressures", *Phys. Review B*, **36**, 6058-6068 (1986).
9. W. A. HARRISON, *Electronic Structure and the Properties of Solids: The Physics of the Chemical Bond*, p. 176, Dover, New York, 1989.
10. S. PLIMPTON, "Fast Parallel Algorithms for Short-Range Molecular Dynamics", *J. Comp. Phys.*, **117**, 1-19 (1995).
11. M. RAZUL, G. MATHAROO, P. POOLE, "Spatial Correlation of the Dynamic Propensity of a Glass-Forming Liquid", *J. Phys.: Condens. Matter*, **23**, 1-9 (2011).

Part IV. *In-Situ* Transmission Electron Microscopy (TEM) Study of Irradiation Response of BN Nanotubes

1. Introduction

Hexagonal Boron Nitride (h-BN), known as “white graphene”, has attracted broad interests due to its superb thermal and chemical stabilities, outstanding mechanical properties and high resistance to oxidation.¹⁻⁹ Boron nitride nanotube (BNNT) is considered as a structural analogue of carbon nanotube (CNT) by alternating B and N atoms to substitute for C atoms¹⁰. Contrary to CNT, BNNT is a wide band gap semiconductor (4.5-5.8 eV¹¹⁻¹³) due to ionic bonding between the atoms. Its electronic properties can be tuned by making hybrid C-BN nanotubes¹⁴, doping or filling with other materials such as metals¹⁵⁻¹⁷, or introducing bending deformation¹⁸. BNNTs with improved band gap have potential applications as electrodes used in semiconductor field (field effect transistor, etc.) performed at high-temperature and hazardous environments, or even under high-dose irradiation environments.

Response of nanostructured materials under irradiation environments is an interesting topic since the irradiation-induced defects can have a great influence on the material properties.¹⁹⁻²¹ The existence of atomic-scale defects in irradiated nanomaterials is responsible for the substantial difference between their theoretically predicted and experimentally measured properties. But irradiation can also be helpful to mechanical strengthening and even to be a powerful tool for engineering the atomic and electronic structures of nanomaterials.²⁰⁻²⁶ Irradiation damage on nanostructured materials will depend on the irradiation source (electron, ion, etc.), the dose and the microstructures of the materials. Electron beam (e-beam) irradiation on multiwalled (MW) CNTs at room temperature resulted in the formation of vacancies on their walls and eventual amorphization under high-dose irradiation.²⁷ It suggested that the atoms sputtered from inner shells remained in the nanotubes and Frenkel pairs created inside the nanotubes could easily recombine. E-beam irradiation on h-BN thin films could generate triangle-shaped vacancy structures,²⁸⁻³¹ which have never been observed in Carbon systems. Nitrogen termination of the edges has been suggested.^{30, 31} These defects may govern the electronic and magnetic properties of h-BN systems.³²⁻³⁴

However, only a few studies about the effects of e-beam irradiation on BNNTs were reported. Neighboring BN divacancies and extended defect lines were observed in single-walled (SW) BNNTs under e-beam irradiation.³⁵ Clustering of multiple vacancies led to extended defects

which locally changed the nanotube diameter and chirality. Long-time irradiation on MW BNNTs resulted in gradual amorphization of BN shells followed with the complete destruction of the nanotube morphology, leaving the material with the consecutive appearance of a near-amorphous BN rod and rectangular onion-like nanoparticle.⁹ Moreover, researchers³⁶ demonstrated to “nanomachine” MW BNNTs to form sharp, crystalline, conical tips and to cut BNNTs for potential applications such as probes for nanomanipulation and imaging¹⁸. However, the mechanism of irradiation damage on MW BNNTs remains unclear, especially about the irradiation-induced vacancy defects.

In this study, in-situ high-resolution transmission electron microscopy (HRTEM) observation directly revealed the nucleation and development of irradiation-induced vacancy defects under extreme parallel e-beam. And we carefully investigated the effects of the e-beam current density and the number of tube wall on the irradiation damage of MW BNNTs.

Experimental methods

The MW BNNTs studied here were grown by thermal chemical vapor deposition (CVD) at 1100-1200 °C.³⁷ The samples for in-situ HRTEM experiments were prepared by depositing BNNTs from a dispersion of nanotubes in ethanol onto the copper grids covered with lacey carbon film (no Formvar).

High energy electron irradiation study was carried out with a probe corrected (monochromator) FEI Titan G² 60-300 kV scanning transmission electron microscope (S/TEM) equipped with an extreme field emission gun (X-FEG) source operated at 80, 200 and 300 keV and a JEOL 2010F transmission electron microscope (TEM) with a Schottky field emission gun (FEG) operating at 200 keV. E-beam current densities used in the experiments were obtained by calculating the counts on the CCD camera for FEI Titan G² 60-300 kV S/TEM and evaluating the values from the previous report³⁸ for JEOL 2010F.

Results and discussion

Microstructure characterization

A SW BNNT can be imaged as a single h-BN sheet rolled up into a seamless molecular cylinder, as shown in Figures 1a and d. Similar to CNT, BNNT also has the chirality, an important geometrical parameter; but for BNNT, the chirality is not directly related to its

electrical properties. The chiral vector (n, m) indicates the direction of the rolling can be obtained as a linear combination of the basis vectors (shown in the inset in Figure 1d): $n \cdot \mathbf{a}_1 + m \cdot \mathbf{a}_2$. The possible chiral vectors for a SW BNNT on a single h-BN sheet can be assigned identically. But for MW BNNTs, they should be composed of many chiral-type SW nanotubes to keep the constant interplanar spacing (~ 0.333 nm from the experimental data).

A TEM image in Figure 1b shows the BNNTs with different diameters and different number of tube walls. The distribution of the number of tube walls is shown in Figure 1c, based on 54 nanotubes we have examined. The number of the tube walls are in the range of 10 to 55 with the average of ~ 26 . Figure 1f shows the BNNT diameter as a function of the number of tube walls. The inner diameters range from 4.8 to 23 nm while the outer diameters from 12 to 55 nm. Note that the inner and outer diameters linearly increase with the number of the tube walls when the number is less than 33. But the tube diameters become randomly distributed when the number is more than 33. The inner diameters are smaller than 23 nm in all the 54 BNNTs. The difference between the outer and inner diameters is always proportional to the number of the tube walls, confirming the constant interplanar spacing in MW BNNTs.

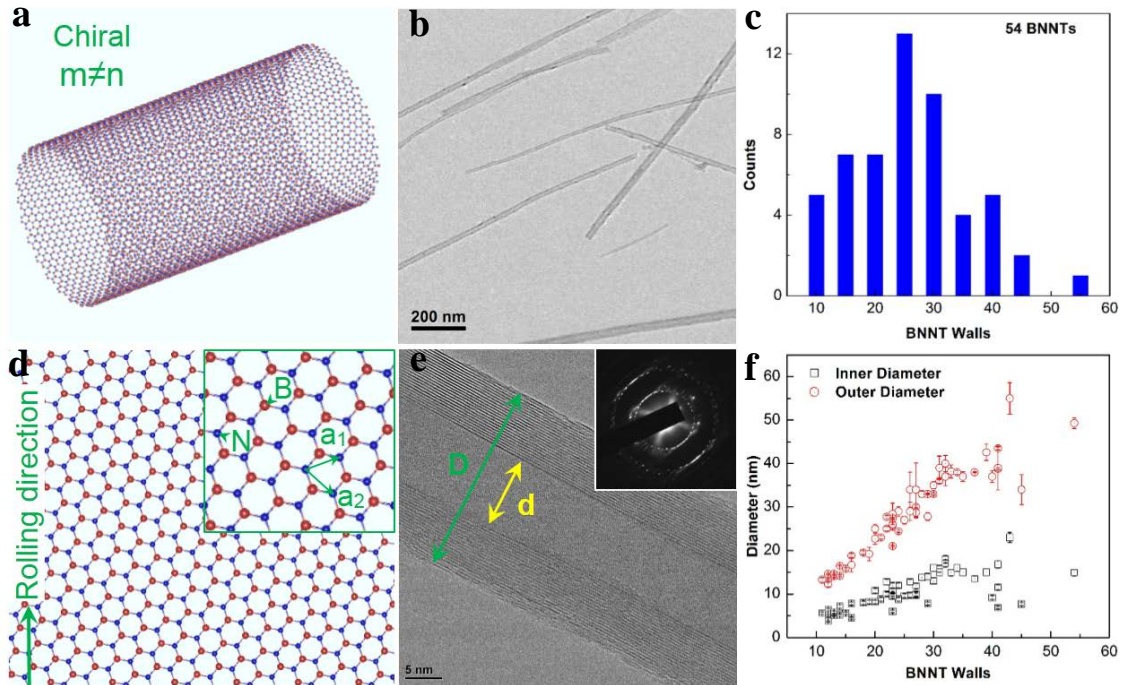


Figure 1. Illustration of SW BNNT (a) rolled by the corresponding sheet (d); Chiral ($m \neq n$). (b) Low magnification and (e) high-resolution TEM images of MW BNNTs. Insets in (e) is the

corresponding SAED pattern. (c) Walls distribution of BNNTs, the average wall of ~ 26 . (d) Distribution of inner and outer diameters (d and D) as a function of BNNT walls

The details of the arrangement of tube walls are shown in Figure 1e, for an individual MW BNNT with ~ 23 walls. The inset in Figure 1e is the corresponding selected-area electron diffraction (SAED) pattern. The interplanar spacing of the neighbor walls, d_{wall} , is measured as ~ 0.333 nm, which is almost the same as the (0002) planar spacing in h-BN at room temperature³⁹. The inner and outer diameters of the nanotubes are labeled as d and D in Figure 1e. Hence, the number of tube walls can also be calculated as, $N = (D-d)/d_{\text{wall}}$. There was a slight difference between the calculated and counted nanotube walls which caused the discrepancy for some of the outer diameters. Those outer diameters were marked with error bars in Figure 1f. The slight deviation of the outer diameter may be due to the shape deformation when transferring the BNNTs onto the copper grids with lacey carbon film.

E-beam irradiation on MW BNNTs

In-situ HRTEM observations in Figure 2 revealed the process of irradiation damage and the evolution of irradiation-induced defects in an individual MW BNNT (~ 32 walls), under an electron energy of 80 keV with a current density of ~ 30 A/cm². The BNNT side walls were damaged layer by layer but there was no obvious shrinkage and collapse about the outer shells until the nanotube was broken. This observation is totally different from the previous results that the MW BNNTs were seriously shrunk under e-beam irradiation³⁶. This difference was mainly caused by the different distribution of e-beam from the two type TEMs (see details in Supplementary Figures S3 and S4). Our in-situ experiments were done under an extreme parallel e-beam with a homogenous distribution of beam intensity. The irradiation damage on the top-bottom layers is as quick as that on the side walls, regardless of the different knock-on direction on the nanotube (Figure 4a). The detailed irradiation process is described as follows (see Supplementary Movie S1). At the initial stage (Figure 2a, 0 min), the nanotube had 32 walls with good atomic arrangement. The marked circles in the insets of Figures 2a and d correspond to the irradiated area (also the beam size). As the time increases, we can clearly observe many irradiation-induced vacancy defects in Figure 2b (20 min). Such vacancy defects have a regular triangular shape which is similar to the previous results in the thin h-BN sheets or membranes

under e-beam irradiation^{29, 30, 40}. It suggested that B atoms were firstly knocked out to form such kind defects since the recent operating electron energy (80 keV) was close the threshold energy (79.5 keV) to knock B out but far away from that (118.6 keV) to knock N out.²⁹⁻³¹ After 45 min (Figure 2c), there were some residual chains on the surface of the nanotube and many of them came out in Figure 2d (60 min). Such chains like curved wires formed by the left part of the outer single layers peeled off from the outer shells during the irradiation. The irradiation damage of the side walls was not homogeneous which could be clearly seen from the rough etching edge. It was due to the damaged voids left by the non-uniform knocked-out atoms at the side walls.

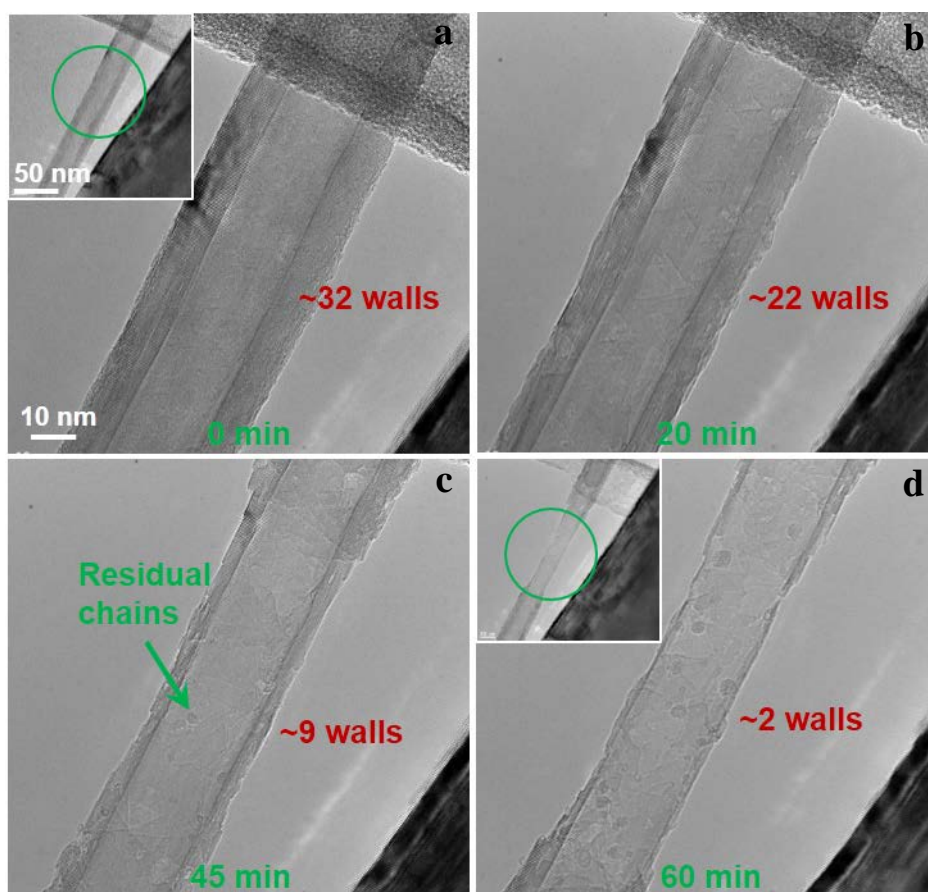


Figure 2. Irradiation damage of an individual MW BNNT (~32 walls). The nanotube walls decreases as the time increases. (a) 0 min, (b) 20 min, (c) 45min and (d) 60 min. Electron energy, 80 keV; current density, $\sim 30 \text{ A/cm}^2$.

Details about the evolution of irradiation-induced vacancy defects are shown in Figure 3. At the early stage (11-17 min, Figure 3a-c), we can clearly see the growth of small triangle-shaped vacancy defects (marked by I-III) and the development of them step by step. Note that all the triangle-shaped vacancy defects were almost aligned to the similar direction, the radial (or rolling) direction. It indicated that the chirality of the outer individual nanotubes were dominated by the armchair type or close to it.

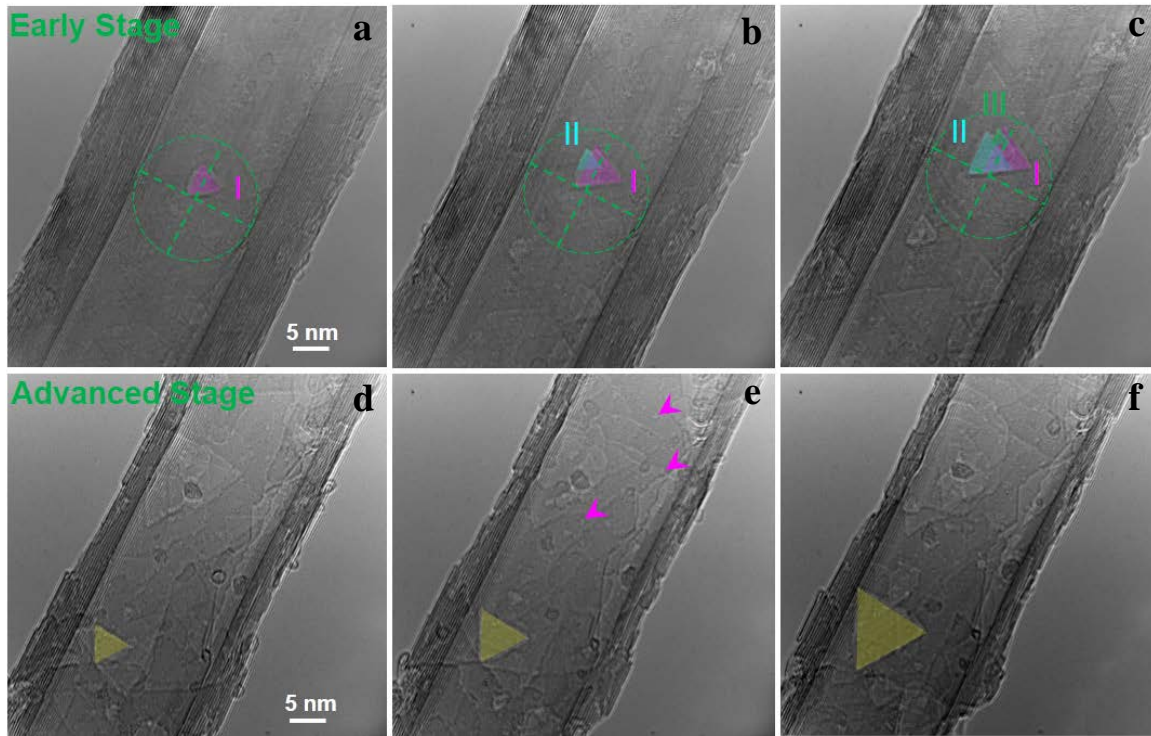


Figure 3. Evolution of irradiation-induced vacancy defects in MW BNNTs. (a-c) the development of triangle-shaped vacancy defects at the early stage (11-17 min); (d-f) the growth of an individual triangle-shaped vacancy defect at the advanced stage (45-47 min). Electron energy, 80 keV; current density, $\sim 30 \text{ A/cm}^2$.

The evolution of the three vacancy defects (marked by I-III in Figure 3a-c) at the early stage can be well illustrated in Figure 4. If only one B atom is knocked out, an individual vacancy will form (Figure 4b). The individual vacancy can grow along two directions which have an included angle of $\sim 30^\circ$ to the tube axis (Z) while not along the other direction perpendicular to the tube axis (Z). The B atoms at the edge plane parallel to the tube axis (labeled as 0° edge in Figure 4b)

seems hard to be knocked out. It is probably due to the stronger bonds between the neighbor B and N atoms at this edge than those at the other two edges (labeled as -60° and 60° edges in Figure 4b), which are weakened by the curvature induced lattice deformation in the nanotube. As described in Figure 3a-c, the vacancy defect (marked by I) only developed to one of the 60° edges (with an included angle of $\sim 60^\circ$ to the tube axis). Therefore, when the individual vacancy in Figure 4b grows, there are two B atoms at the 60° edge needed to be knocked out (Figure 4c). After that, the singular N atom will be unstable and also be knocked off (Figure 4c). It should be mentioned that the atoms at the -60° edge have the same possibility to be knocked out but it does not happen. A theoretical study³⁵ predicted that the bonds of atoms neighboring to the vacancy would be reconstructed due to the curvature induced lattice deformation. In our case, the reconstructed structure around the vacancy would be asymmetrical, which caused the growth of the vacancy defects along a special direction and expanded at the same direction, as shown in Figure 4d. Interestingly, a new triangle-shaped vacancy defect (marked by II in Figure 3b and 4e) came out at the side of the stable vacancy defect I. The nucleation of such vacancies was due to the randomly knocked-out B atoms, but the growth of them was along the direction (marked in Figure 4e) to the -60° edge of vacancy defect I. The possible reason is that the bonds of B and N atoms at the area close to defect I lose the equilibrium state due to the generation of defect II, which will cause that the related B atoms are easily knocked off. When the -60° edge of defect II encountered to the edge of defect I, defect II stopped to grow and would emerge into defect I late. Furthermore, another small vacancy defect (marked by III in Figure 3c and 4f) was observed to stay at the corner between defect I and II. But it could not grow too much since it was constrained by the other two. And it quickly emerged into defect I and II. After that, the three vacancy defects formed a bigger one which expanded across to the whole top surface (see Supplementary Movie S1). Accordingly, it can be concluded that the nucleation of vacancy defects follow the rule that the B atoms will be first knocked out to form triangle-shaped vacancies and then the vacancy defects will grow along a special direction step by step.

On the other hand, the development of an individual triangle-shaped vacancy defect was recorded at the advanced stage (45-47 min, Figure 3d-f). It gradually grew along a special direction (marked in Figure 3d) step by step as the irradiation time increased. Note that any edge of the triangle was away from the tube growth direction or radial direction. It suggests that the chirality of such sub-nanotubes should be dominated by the chiral type which was different from

those at the early stage (Figure 3a-c). Additionally, there were many small white spots (some of them marked by the arrows in Figure 3b) on the top surface of the outer shells, which were the vacancies caused by knocking-out the B atoms from the in-plane lattice. Here the thickness of the nanotube along the incident e-beam direction was well reduced by the e-beam so that we could directly observe them. Consequently, under 80 keV irradiation, individual vacancies will be first induced by knocking-out the B atoms at the outer walls of BNNTs, and then triangle-shaped vacancy defects will be developed and expanded as the irradiation time increases.

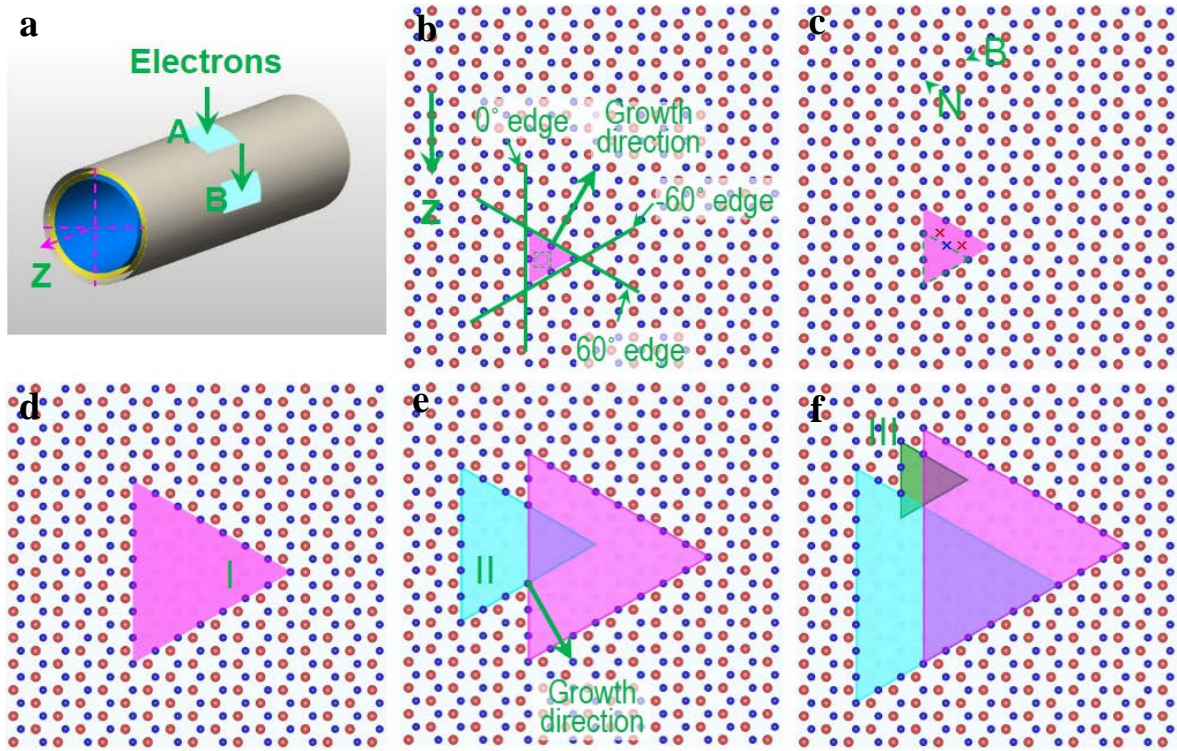


Figure 4. Illustrations to the evolution of irradiation-induced vacancy defects in MW BNNTs. (a) A schematic map showing a MW BNNT under the incident electron beam. (b-f) Atomic models to show the nucleation and propagation of irradiation-induced vacancies.

The e-beam irradiation damage are related to the electron energy, the electron flux, the studied structure and the irradiation time. Here we further investigated the effects of different e-beam current density and the number of tube wall on the damage processes by in-situ HRTEM experiments, as shown in Figure 5a and b, respectively. The electron energy in all experiments was fixed to 80 keV, which is the favorable value to observe the irradiation-induced vacancy

defects in MW BNNTs. The reduction of the BNNT walls was plotted as a function of the irradiation time (Figure 5). Note that the reduction of the tube walls (N) is normalized to the initial walls (N_0) of MW BNNTs. It is clear to see in Figure 5a and b that the reduction of tube walls is slowly changed at the primary stage and then almost a linear change as the time increases, whatever the current density and the nanotube wall change.

However, the reduction speed of nanotube walls will increase with the increase of the current density, from 14 to 84 A/cm², as shown in Figure 5a. The time for the total damage (nanotube broken) decreases as the current density increases. The damage speed changes regularly when the current density is above 30 A/cm². But it will decrease a lot when the current density is less than 30 A/cm².

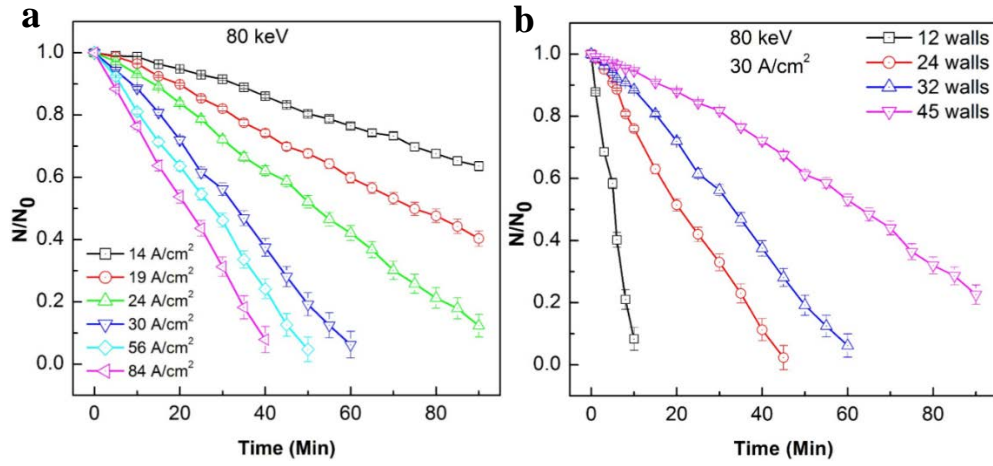


Figure 5. The reduction of BNNT walls as a function of irradiation time. The reduction is normalized to the initial walls of BNNTs. **(a)** Under different current densities; **(b)** BNNTs with different walls under the same current density (30 A/cm²).

The effects of e-beam current density on the microstructure evolution were illustrated in Figure 6. Figures 6a-c show the BNNTs under a current density of 56 A/cm². Both triangle- (marked by I and II) and polygon-shaped (marked by III) vacancy defects were induced in the nanotube. They grew bigger and bigger as the irradiation time increased. But in Figures 6d-f, only irregular polygon-shaped vacancy defects were observed which was due to the higher electron flux (84 A/cm²). Comparison of the three chosen current densities (30, 56 and 84 A/cm²), it is clear that the shape of irradiation-induced vacancy defects will develop from regular triangle to irregular polygon as the e-beam current density increases. Accordingly, if the current

density is less than 30 A/cm^2 , there is only triangle-shaped vacancy defects caused by knocking the B atoms out. The generation of vacancies will be quickly slowed down as the decrease of current density and the damage speed is decreased (Figure 5a). Whereas the current density is more than 30 A/cm^2 , the speed of knocking-out of B atoms is continually increased as the increase of current density and the damage speed is also increased (Figure 5a).

On the other hand, under the same e-beam energy (80 keV and 30 A/cm^2), the thin BNNTs (~ 12 walls) will be much easier to be damaged as compared to the thicker ones, shown in Figure 5b. The one with 45 walls needs ~ 120 min to be totally damaged which is twelve times than that of the thin one with 12 walls. Note that we only take into account of the damage of the side walls. As the tube wall increases, the thickness of the side wall also increases, which is due to the increase of the outer diameter of the nanotube (Figure 1d). It will directly extend the damage process (the time of knocking-out atoms) because the irradiation damage is from top to bottom. It suggests that the increase of nanotube walls will be helpful to improve the radiation tolerance of BNNTs.

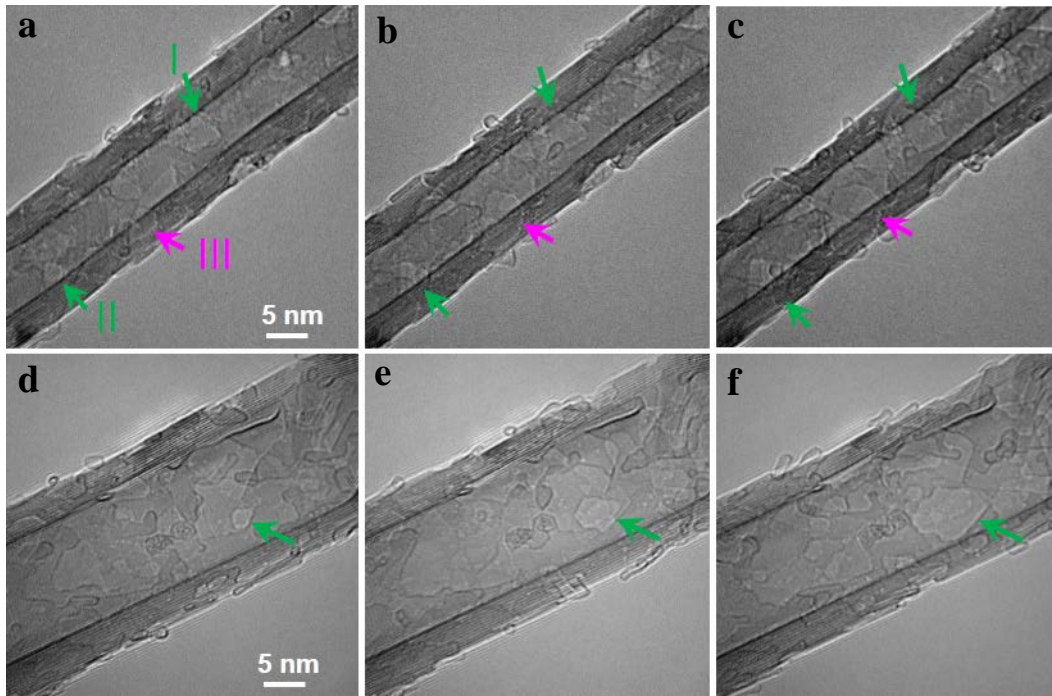


Figure 6. Illustrations to the evolution of irradiation-induced vacancy defects in MW BNNTs as the current density changes. (a-c) 56 A/cm^2 , 17-19 min; (d-f) 84 A/cm^2 , 22-24 min.

Conclusions

Evolution of irradiation-induced defects in MW BNNTs was systematically studied under extreme parallel e-beam (80 keV), including the effects of e-beam current density and nanotube wall on the irradiation damage. Under a mediate e-beam current density (30 A/cm^2), irradiation-induced vacancy defects with triangular shape were widely observed in MW BNNTs. Triangular vacancies nucleated and developed step by step, and layer by layer by knocking the B atoms out during the irradiation. As the increase of current density, the shape of irradiation-induced vacancy defects would develop from regular triangle to irregular polygon.

The irradiation damage on MW BNNTs was going through layer by layer, from outer to inner layers. The irradiation damage of top-bottom layers was as quick as that of the side walls, regardless of the different knock-on directions. The increase of nanotube walls would directly enhance the radiation tolerance of BNNTs.

This study will open the mind to the researchers to further understand the microstructure evolution in MW BNNTs and explore the effects of irradiation-induced defects on the physical and mechanical properties of MW BNNTs under irradiation environments.

References

1. Golberg, D.; Bando, Y.; Tang, C. C.; Zhi, C. Y., Boron Nitride Nanotubes. *Advanced Materials* **2007**, *19* (18), 2413-2432.
2. Zhi, C.; Bando, Y.; Tang, C.; Golberg, D., Boron nitride nanotubes. *Materials Science and Engineering: R: Reports* **2010**, *70* (3–6), 92-111.
3. Golberg, D.; Bando, Y.; Huang, Y.; Terao, T.; Mitome, M.; Tang, C.; Zhi, C., Boron Nitride Nanotubes and Nanosheets. *ACS Nano* **2010**, *4* (6), 2979-2993.
4. Arenal, R.; Blase, X.; Loiseau, A., Boron-nitride and boron-carbonitride nanotubes: synthesis, characterization and theory. *Advances In Physics* **2010**, *59* (2), 101-179.
5. Zeng, H.; Zhi, C.; Zhang, Z.; Wei, X.; Wang, X.; Guo, W.; Bando, Y.; Golberg, D., “White Graphenes”: Boron Nitride Nanoribbons via Boron Nitride Nanotube Unwrapping. *Nano Letters* **2010**, *10* (12), 5049-5055.
6. Wang, J.; Lee, C. H.; Yap, Y. K., Recent advancements in boron nitride nanotubes. *Nanoscale* **2010**, *2* (10), 2028-2034.
7. Ci, L.; Song, L.; Jin, C.; Jariwala, D.; Wu, D.; Li, Y.; Srivastava, A.; Wang, Z. F.; Storr, K.; Balicas, L.; Liu, F.; Ajayan, P. M., Atomic layers of hybridized boron nitride and graphene domains. *Nat Mater* **2010**, *9* (5), 430-435.
8. Chopra, N. G.; Luyken, R. J.; Cherrey, K.; Crespi, V. H.; Cohen, M. L.; Louie, S. G.; Zettl, A., Boron Nitride Nanotubes. *Science* **1995**, *269* (5226), 966-967.
9. Golberg, D.; Bando, Y.; Han, W.; Bourgeois, L.; Kurashima, K.; Sato, T., Multi-and Single-Walled Boron Nitride Nanotubes Produced From Carbon Nanotubes by a Substitution Reaction. *MRS Online Proceedings Library* **1999**, *593*, null-null.
10. Krivanek, O. L.; Chisholm, M. F.; Nicolosi, V.; Pennycook, T. J.; Corbin, G. J.; Dellby, N.; Murfitt, M. F.; Own, C. S.; Szilagyi, Z. S.; Oxley, M. P.; Pantelides, S. T.; Pennycook, S. J., Atom-by-atom structural and chemical analysis by annular dark-field electron microscopy. *Nature* **2010**, *464* (7288), 571-574.
11. Arenal, R.; Stéphan, O.; Kociak, M.; Taverna, D.; Loiseau, A.; Colliex, C., Electron Energy Loss Spectroscopy Measurement of the Optical Gaps on Individual Boron Nitride Single-Walled and Multiwalled Nanotubes. *Physical Review Letters* **2005**, *95* (12), 127601.
12. Wang, J.; Kayastha, V. K.; Yap, Y. K.; Fan, Z.; Lu, J. G.; Pan, Z.; Ivanov, I. N.; Puretzky, A. A.; Geohegan, D. B., Low Temperature Growth of Boron Nitride Nanotubes on Substrates. *Nano Letters* **2005**, *5* (12), 2528-2532.
13. Czerw, R.; Webster, S.; Carroll, D. L.; Vieira, S. M. C.; Birkett, P. R.; Rego, C. A.; Roth, S., Tunneling microscopy and spectroscopy of multiwalled boron nitride nanotubes. *Applied Physics Letters* **2003**, *83* (8), 1617-1619.
14. Golberg, D.; Bando, Y.; Dorozhkin, P.; Dong, Z.-C., Synthesis, Analysis, and Electrical Property Measurements of Compound Nanotubes in the B-C-N Ceramic System. *MRS Bulletin* **2004**, *29* (01), 38-42.
15. Chen, H.; Chen, Y.; Li, C. P.; Zhang, H.; Williams, J. S.; Liu, Y.; Liu, Z.; Ringer, S. P., Eu-doped Boron Nitride Nanotubes as a Nanometer-Sized Visible-Light Source. *Advanced Materials* **2007**, *19* (14), 1845-1848.
16. Xiang, H. J.; Yang, J.; Hou, J. G.; Zhu, Q., Half-metallic ferromagnetism in transition-metal encapsulated boron nitride nanotubes. *New Journal of Physics* **2005**, *7* (1), 39.
17. Golberg, D.; Xu, F. F.; Bando, Y., Filling boron nitride nanotubes with metals. *Appl Phys A* **2003**, *76* (4), 479-485.

18. Ghassemi, H. M.; Lee, C. H.; Yap, Y. K.; Yassar, R. S., Field emission and strain engineering of electronic properties in boron nitride nanotubes. *Nanotechnology* **2012**, 23 (10), 105702.
19. Krasheninnikov, A. V.; Nordlund, K., Ion and electron irradiation-induced effects in nanostructured materials. *Journal of Applied Physics* **2010**, 107 (7), -.
20. Krasheninnikov, A. V.; Banhart, F., Engineering of nanostructured carbon materials with electron or ion beams. *Nat Mater* **2007**, 6 (10), 723-733.
21. Kis, A.; Csanyi, G.; Salvétat, J. P.; Lee, T.-N.; Couteau, E.; Kulik, A. J.; Benoit, W.; Brugger, J.; Forro, L., Reinforcement of single-walled carbon nanotube bundles by intertube bridging. *Nat Mater* **2004**, 3 (3), 153-157.
22. Radosavljević, M.; Appenzeller, J.; Derycke, V.; Martel, R.; Avouris, P.; Loiseau, A.; Cochon, J.-L.; Pigache, D., Electrical properties and transport in boron nitride nanotubes. *Applied Physics Letters* **2003**, 82 (23), 4131-4133.
23. Cumings, J.; Zettl, A., Field emission and current-voltage properties of boron nitride nanotubes. *Solid State Communications* **2004**, 129 (10), 661-664.
24. Lehtinen, O.; Nikitin, T.; Krasheninnikov, A. V.; Sun, L.; Banhart, F.; Khriachtchev, L.; Keinonen, J., Characterization of ion-irradiation-induced defects in multi-walled carbon nanotubes. *New Journal of Physics* **2011**, 13 (7), 073004.
25. Peng, B.; Locascio, M.; Zapol, P.; Li, S.; Mielke, S. L.; Schatz, G. C.; Espinosa, H. D., Measurements of near-ultimate strength for multiwalled carbon nanotubes and irradiation-induced crosslinking improvements. *Nat Nano* **2008**, 3 (10), 626-631.
26. Mikó, C.; Milas, M.; Seo, J. W.; Couteau, E.; Barišić, N.; Gaál, R.; Forró, L., Effect of electron irradiation on the electrical properties of fibers of aligned single-walled carbon nanotubes. *Applied Physics Letters* **2003**, 83 (22), 4622-4624.
27. Banhart, F., Irradiation effects in carbon nanostructures. *Reports on Progress in Physics* **1999**, 62 (8), 1181.
28. Zobelli, A.; Gloter, A.; Ewels, C. P.; Colliex, C., Shaping single walled nanotubes with an electron beam. *Physical Review B* **2008**, 77 (4).
29. Meyer, J. C.; Chuvilin, A.; Algara-Siller, G.; Biskupek, J.; Kaiser, U., Selective Sputtering and Atomic Resolution Imaging of Atomically Thin Boron Nitride Membranes. *Nano Letters* **2009**, 9 (7), 2683-2689.
30. Jin, C.; Lin, F.; Suenaga, K.; Iijima, S., Fabrication of a Freestanding Boron Nitride Single Layer and Its Defect Assignments. *Physical Review Letters* **2009**, 102 (19), 195505.
31. Kotakoski, J.; Jin, C. H.; Lehtinen, O.; Suenaga, K.; Krasheninnikov, A. V., Electron knock-on damage in hexagonal boron nitride monolayers. *Physical Review B* **2010**, 82 (11), 113404.
32. Barone, V.; Peralta, J. E., Magnetic Boron Nitride Nanoribbons with Tunable Electronic Properties. *Nano Letters* **2008**, 8 (8), 2210-2214.
33. Schmidt, T. M.; Baierle, R. J.; Piquini, P.; Fazzio, A., Theoretical study of native defects in BN nanotubes. *Physical Review B* **2003**, 67 (11), 113407.
34. Wei, X.; Tang, D.-M.; Chen, Q.; Bando, Y.; Golberg, D., Local Coulomb Explosion of Boron Nitride Nanotubes under Electron Beam Irradiation. *ACS Nano* **2013**, 7 (4), 3491-3497.
35. Zobelli, A.; Ewels, C. P.; Gloter, A.; Seifert, G.; Stephan, O.; Csillag, S.; Colliex, C., Defective Structure of BN Nanotubes: From Single Vacancies to Dislocation Lines. *Nano Letters* **2006**, 6 (9), 1955-1960.

36. Celik-Aktas, A.; Stubbins, J. F.; Zuo, J.-M., Electron beam machining of nanometer-sized tips from multiwalled boron nitride nanotubes. *Journal of Applied Physics* **2007**, *102* (2), -.
37. Lee, C. H.; Wang, J.; Kayatsha, V. K.; Huang, J. Y.; Yap, Y. K., Effective growth of boron nitride nanotubes by thermal chemical vapor deposition. *Nanotechnology* **2008**, *19* (45), 455605.
38. Xu, W.; Zhang, Y.; Cheng, G.; Jian, W.; Millett, P. C.; Koch, C. C.; Mathaudhu, S. N.; Zhu, Y., In-situ atomic-scale observation of irradiation-induced void formation. *Nature Communications* **2013**, *4*.
39. Paszkowicz, W.; Pelka, J. B.; Knapp, M.; Szyszko, T.; Podsiadlo, S., Lattice parameters and anisotropic thermal expansion of hexagonal boron nitride in the 10–297.5 K temperature range. *Appl Phys A* **2002**, *75* (3), 431-435.
40. Okada, S., Atomic configurations and energetics of vacancies in hexagonal boron nitride: First-principles total-energy calculations. *Physical Review B* **2009**, *80* (16), 161404.